Cold dense 2-colour spectroscopy.

Sitch, Peter D

Cold Dense 2-Colour Spectroscopy

Peter D. Sitch

Submitted to the University of Wales in fulfilment
of the requirements for the Degree of

Doctor of Philosophy

Swansea University

2009

Abstract

The particle spectrum of SU(2) lattice gauge theory with two flavours of Wilson quark is studied on an $8^3 \times 16$ lattice using all-to-all propagators for the quark states and a diagonalised set of smeared plaquette operators for the gluonic states. Particular emphasis is put on each state's dependence on quark chemical potential μ. As μ is increased from zero the diquark states with non-zero baryon number B respond as expected, while states with $B = 0$ remain unaffected until the onset of non-zero baryon density at $\mu = m_\pi/2$ is reached. Post onset the pion becomes heavier in accordance with chiral perturbation theory while the rho becomes lighter. In the diquark sector a Goldstone state associated with a superfluid ground state can be identified. A further consequence of superfluidity is an approximate degeneracy between mesons and baryons with the same spacetime and isospin quantum numbers. Tentative evidence for the binding of states with kaon quantum numbers within the baryonic medium. In the glueball sector the properties of the lightest scalar and tensor states are studied. The amplitudes of each state exhibit different behaviour in vacuum, onset and a high μ phase. The scalar mass is observed to remain constant in the vacuum and the superfluid phases, but shows sensitivity to onset through a mass dip, and becomes heavy in the high μ phase. The tensor mass is in general difficult to resolve in the vacuum phase but appears to becomes lighter post onset.

DECLARATION

This work has not previously been accepted in substance for any degree and is not being concurrently submitted in candidature for any degree.

Signed ..... (candidate)

Date: 26th August 2009

STATEMENT 1

This thesis is the result of my own investigations, except where otherwise stated. Where correction services have been used, the extent and nature of the correction is clearly marked in a footnote(s).

Other sources are acknowledged by footnotes giving explicit references. A bibliography is appended.

Signed ..... (candidate)

Date: 26th August 2009

STATEMENT 2

I hereby give consent for my thesis, if accepted, to be available for photocopying and for inter-library loan, and for the title and summary to be made available to outside organisations.

Signed ..... (candidate)

Date: 26th August 2009

Contents

1 Introduction **1**

1.1 Extreme QCD 1

1.2 Outline and Aims 5

1.3 Lattice QCD 5

1.3.1 Discretising QCD 7

1.4 Dense Lattice QCD 13

1.5 Non-zero μ Methods: Dodging the Sign Problem 15

1.5.1 Multiparameter Reweighting 16

1.5.2 Finite Density by Taylor Expansion 17

1.5.3 QCD at Imaginary μ 17

1.5.4 Canonical Ensemble Method 18

1.5.5 An Overview and a New Approach 19

2 2-Colour QCD **20**

2.1 Introduction to 2-Colour Quantum Chromodynamics 20

2.1.1 The Phase Diagram 23

2.2 The 2-Colour Collaboration 25

2.3 The 2cQCD Action 26

2.3.1 Physical limits and Problems with High μ 29

3 Discussion of the Applied Techniques **30**

3.1 Spectroscopy 30

3.1.1 Fermionic Correlators 32

3.2 All-to-All Propagators 33

3.2.1 Simple All-to-All Propagators 34

3.2.2 Dublin Dilution Method 35

3.2.3 So Why All-to-All for Us? 39

3.3 Glueball Techniques 40

3.3.1 Simple to Formulate; Hard to Measure 40

3.3.2 Building a Better Operator: Smearing 42

3.3.3 Optimal Operator Choice 46

3.4 Numerical Techniques 47

3.4.1 Jackknife Error Estimation 47

3.4.2 Autocorrelation and Binning 49

4 The Hadronic Spectrum **53**

4.1 Construction of Hadronic Correlators 53

4.1.1 Fermion Propagators 53

4.1.2 Mesons 55

4.1.3 Diquarks 56

4.2 Numerical Method 59

4.3 Results 60

4.4 Discussion 74

5 Glueball Studies and Results **76**

5.1 Numerical Methods 76

5.1.1 Smearing Analysis and Operator Construction 77

5.1.2 Resolving The Vacuum 81
5.1.3 Scaling with the Diquark Source 85
5.2 Results 85
5.2.1 Glueball Amplitudes 86
5.2.2 The Scalar Glueball Mass 88
5.2.3 The Tensor Glueball Mass 92
5.3 Discussion and Outlook 92

6 Conclusions **95**

Acknowledgements

I would like to acknowledge the work and patience of my supervisor Simon Hands. Thanks also to Jon-Ivar Skullerud who provided the initial code and the kick to use it, and Chris Allton for his support and mentoring during the corrections. Finally I'd like to thank Fran Ling who tried to keep me sane.

List of Figures

1.1 A cartoon of a proposed QCD phase diagram 3

1.2 The gauge-invariant plaquette operator $U_{\mu\nu}(x)$ 9

2.1 Proposed phase diagram for 2 colour QCD 24

2.2 Figure taken from [1] showing χPT predictions for the chiral multiplet for $\mu \neq 0$ 27

3.1 Plot of pion effective mass from point-to-all and all-to-all propagators 38

3.2 Zero time correlator $C(0)$ for the 0^{++} glueball state at $\mu = 0, j = 0.04$ 44

3.3 Effective mass plot for the 0^{++} glueball state at $\mu = 0, j = 0.04$ 45

3.4 Autocorrelation and binning errors for 0^{++} amplitude and average spatial plaquette at $\mu = 0$ 51

4.1 Isoscalar scalar diquark correlators for $\mu a = 0.0 - 0.5$ 61

4.2 Pi and rho masses as a function of diquark source strength j . 62

4.3 Meson masses as a function of μ for $ja = 0.04$ 63

4.4 Higgs and Goldstone masses as a function of μ 65

4.5 Diquark masses as a function of μ 67

4.6 Comparison between the Higgs, Goldstone and isoscalar diquark results 68

4.7 Diquarks and meson states overlaid to observe meson-baryon degeneracy 70

4.8 Results of partial quenching in κ 71

4.9 Kaon spectrum as a function of μ 72

5.1 Effects of APE smearing on $C(0)$ for the basic 0^{++} operator . 78

5.2 Effects of smearing on the $\mu = 0$ 0^{++} effective mass, m_{eff} . . . 80

5.3 The average spatial plaquette, $\langle\phi\rangle$ as a function of μ at $N_S = 4\lambda = 0.15$ 82

5.4 Plot of $\mu = 0.35, 0.38$ basic 0^{++} correlators and fits with a free constant included 84

5.5 0^{++} and 2^{++} amplitudes as a function of μ 87

5.6 0^{++} masses as a function of μ from cosh fits 89

5.7 0^{++} correlators at $\mu = 0.50$ and $\mu = 0.52$ 90

5.8 0^{++} masses as a function of μ from cosh fits with an additional constant parameter 91

5.9 2^{++} masses as a function of μ from cosh fits 93

Chapter 1

Introduction

1.1 Extreme QCD

Quantum chromodynamics, QCD, describes the hadronic sector of the standard model and its interactions through the strong force. The fermionic quarks and the gauge bosons, the gluons, are its fundamental degrees of freedom. Despite being well established (QCD was first formulated in 1972 by Harold Fritzsch, Murray Gell-Mann and Heinrich Leutwyler [2]) it is by no means fully understood. Large regions of its parameter space remain relatively unexplored and solutions to the big questions of colour confinement are still currently beyond reach. One of the defining properties of QCD is that it becomes asymptotically free at high energies and therefore the standard perturbative quantum field theory techniques are very successful in such regimes, with accurate predictions of phenomena such as jet production. In the low energy sector however, the coupling becomes strong and these techniques are no longer appropriate. A solution is to discretise spacetime and simulate QCD on the lattice using computational techniques. Such an approach has proved very useful as it is fully non-perturbative.

In order to study the formation of the early universe and the properties of astrophysical phenomena, QCD can be applied in regimes far from that of

ordinary hadronic matter. Such applications clearly test both the validity of the theory and vastly increase the understanding of its phase space. A suitable framework to house such extreme environments would be the thermodynamic properties of quark matter, that is, the phase diagram of QCD with temperature T against chemical potential μ_B (see figure 1.1). Due to asymptotic freedom the regions of this diagram which are best known, apart from normal nuclear matter, are those of either extreme high temperature or extreme high density.

At some high temperature entropy will preclude any pattern of order and the dominant degrees of freedom will become the bare quarks and gluons. This is clearly a very different from the low temperature ground state which is dominated by the pions. Since the entire $\mu_B = 0$ axis is accessible to lattice simulations much work has been done studying this transition, and whilst it has generally been shown to be to be a crossover [3] there is still some controversy about the precise temperature at which it occurs [4, 5]. Heavy ion collision experiments, which probe close to this axis, have begun to see the signs of such a phase transition and the existence of this new form of matter [6, 7, 8, 9]. The resultant sea of interacting particles is known as the quark-gluon plasma and its properties obviously have huge implications for the understanding of the early universe.

At extreme high density, it can be argued that the quarks are weakly interacting[1] and so will form a Fermi surface. The dominant behaviour of the system is then only determined by the quarks lying on or close to the surface. Such a system is unstable to an attractive interaction between quarks at the surface, and so in analogy with BCS theory, diquark condensation is predicted, which would spontaneously break local symmetries of the ground state creating a colour superconducting phase. For example, the ground state of QCD with 3 flavors of light quark at low temperature and asymptotically high density is thought to exhibit a form of colour superconductivity know as a "colour-flavour locked" (CFL) state in which the

[1]Naïvely, high densities imply interactions on short distance scales, which therefore implies weak coupling.

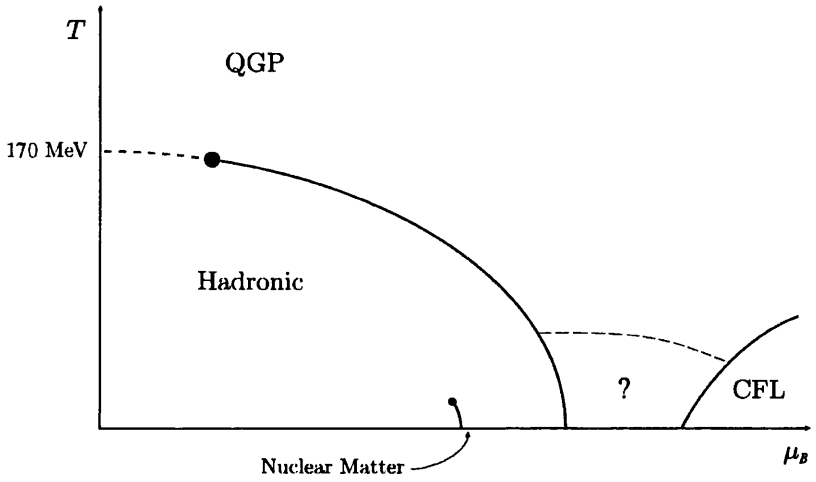

Figure 1.1: A cartoon of a proposed QCD phase diagram, with temperature and baryon chemical potential on the axes. Solid lines indicate areas of phase coexistence, filled circles critical points and dotted lines areas of crossover. By moving up the temperature axis at $\mu_B = 0$, the crossover region between the hadronic phase and the QGP phase is observed at $T \sim 170$ MeV. If on the other hand the μ_B is increased for $T = 0$ the onset of nuclear matter in the hadronic phase occurs at $\mu_B \sim 922$ MeV. For very large μ_B it has been determined that QCD is in a "colour-flavour-locked" superconducting phase where the three light quark species condense into Cooper pairs. The phase between these two regions is currently not very well understood with many ground states proposed. Neutron star cores live somewhere here.

$SU(3)_c \times SU(N_f)_L \times SU(N_f)_R \times U(1)_B$ symmetry is spontaneously broken in the colour anti-triplet channel to a diagonal $SU(3)_\Delta$. Such a phase is simultaneously colour superconducting, superfluid, and chirally broken [10, 11]. Since diquark condensation is thought to occur via a BCS mechanism, it can be accurately described by a self-consistent gap equation when the QCD coupling is weak, i.e. in the asymptotic regime $\mu_B \to \infty$, where μ_B is the quark chemical potential or Fermi energy [12]. This gap equation solves for the smallest energy 2Δ required to excite a quasiparticle pair out of the filled Fermi sea ground state. Solutions with $\Delta > 0$ imply the instability of a sharp Fermi surface with respect to formation of a condensate of Cooper pairs, and hence BCS-esque superconductivity. However, the required densities to make such a technique viable are much greater than those thought to occur in our universe, the densest candidates being the centres of compact stars which are estimated to have a baryon chemical potential of the order of 1 GeV [13].

Therefore in this physically interesting regime, QCD is strongly interacting and perturbative techniques fail. At these less than asymptotic densities another complicating factor is that the strange quark mass is no longer necessarily negligible compared to μ_B. Hence other channels involving pairing between just the u and d quarks may be preferred. This has led to the proposal of many different possible ground states, including pairing just between the two light flavours (2CS theory) and crystalline examples which are analogous to the LOFF phases in conventional superconductivity [14, 15].

The central tool in the non-perturbative analysis of low energy QCD, the numerical studies of lattice QCD, is unfortunately not viable in such a regime of large μ, as will be explained in section 1.4. Currently, analytic studies of these regimes must either use some approximate non-perturbative approach such as the instanton liquid [16], or resort to phenomenological models of the strong interaction such as QCD with an SU(2) gauge group [17, 18, 19] and the Nambu - Jona-Lasinio (NJL) model [20, 21].

1.2 Outline and Aims

This work aims to study the low temperature particle spectrum of lattice 2-colour QCD and its response to a non-zero chemical potential. The hope is that such information would improve the understanding of the theory's phase structure, which beyond the predictions of chiral perturbation theory, is poorly understood. There is a wish to find possible implications for full QCD at high density, and useful study of the techniques required to make such measurements.

A brief overview of the formulation of lattice QCD is given in the remainder of this chapter, where the current problems associated with dense simulations are detailed. Examples of techniques used to sidestep these problems to explore small μ/T are also given. Chapter 2 gives a basic introduction to 2-colour quantum chromodynamics, its phase structure and the precise action that has been studied. Chapter 3 discusses the more advanced techniques used to study the particle spectrum, which include all-to-all propagators, the creation and optimisation of glueball operators and the treatment of jackknife errors and autocorrelations. The hadron results are presented in chapter 4, and the meson and diquark spectra discussed. The Higgs and Goldstone modes of the superfluid phase are identified, and kaonic states are constructed and simulated. In the second results chapter, the properties of the scalar and tensor glueball are explored as a function of the applied chemical potential. The final chapter summarises the work of this thesis and discusses the outlook for future directions.

1.3 Lattice QCD

Lattice QCD is the quantum field theory of quantum chromodynamics formulated on a discrete spacetime lattice. This approximation allows powerful analytical and numerical techniques to be applied, and the non-perturbative properties of the theory to be explored. It has proven to be useful framework

to study phenomena such as confinement and quark-gluon plasma formation.

Continuum QCD: Definition

The Lagrange density for continuum Euclidean QCD is

$$\mathcal{L}_{QCD} = \sum_{i=1}^{N_f} [\bar{\psi}_i(x)(\not{D} + m_i)\psi_i(x)] + \frac{1}{4}F_{\mu\nu}F^{\mu\nu} \tag{1.1}$$

where $\psi_i(x)$ is the Grassmann valued fermion field corresponding to a quark of flavour i and with mass m_i; the Dirac matrix $\not{D} = \gamma^\mu[\partial_\mu - igA_\mu(x)]$; and $A_\mu(x)$ is the gluon field which can be decomposed into components as

$$A_\mu(x) = \sum_a \lambda^a A^a_\mu(x). \tag{1.2}$$

The field strength tensor is given by

$$F^a_{\mu\nu} = \partial_\mu A^a_\nu - \partial_\nu A^a_\mu + g f_{abc} A^b_\mu A^c_\nu \tag{1.3}$$

The generators of the colour gauge group are the traceless Hermitian λ^a matrices and f_{abc} are the structure constants.

The Partition Function

The starting point for lattice QCD is not the Lagrangian however, but the partition function Z in Euclidean spacetime. This enables Euclidean quantum field theory to make contact with statistical mechanics and is nothing more than the Feynman path integral over all the degrees of freedom of the system.

$$Z = \int \mathcal{D}A_\mu \, \mathcal{D}\psi \, \mathcal{D}\bar{\psi} \, e^{-\mathcal{L}_{QCD}} \tag{1.4}$$

where S is the QCD action

$$\mathcal{S} = \int d^4x \, \mathcal{L}_{QCD} \tag{1.5}$$

which contains the previously defined Lagrangian. Note that unlike in Minkowski space, the fermionic fields ψ and $\bar{\psi}$ are independent. They can be integrated out exactly because of their Grassmann nature with the result

$$Z = \int \mathcal{D}A_\mu \, \mathrm{det}M \; e^{\int d^4x \; (-\frac{1}{4}F_{\mu\nu}F^{\mu\nu})}. \tag{1.6}$$

where M is the quark matrix, $M = \not{D} + m_i$. These fermionic contribution is now contained in the highly non-local term $\mathrm{det}M$, and the partition function is an integral over background gauge configurations. It can be useful to define an effective action by rewriting the determinant in the exponential, giving

$$S_{eff} = S_{gauge} + S_{quarks} = \int d^4x \; (\frac{1}{4}F_{\mu\nu}F^{\mu\nu}) - \sum_i \log(\mathrm{Det}M_i) \tag{1.7}$$

where the sum is taken over the quark flavors.

Results for physical observables can then be obtained by calculating expectation values

$$\langle \mathcal{O} \rangle = \frac{1}{Z} \int \mathcal{D}A_\mu \; \mathcal{O} \; e^{-S_{eff}} \; . \tag{1.8}$$

where $\mathcal{O}$ is an operator expressed in terms of products of gauge and quark fields. To eliminate this dynamical quark dependence, the fermion fields are in general re-expressed using Wick contraction as propagators.

1.3.1 Discretising QCD

The prescription for discretising QCD was provided by Wilson [22] in 1974 when he defined an action on a discrete space-time lattice with spacing a. This serves two purposes: first, if the lattice is introduced in a finite volume, the number of integration variables becomes finite and the integrals become

well defined. Second, the lattice regulator introduces an ultraviolet cutoff at the scale of the inverse lattice spacing $1/a$ and thus helps to regulate the theory. Such discretisation will necessarily break symmetries of the theory, however the construction is such that these symmetries will be recovered in the continuum limit $a \to 0$.

The quark fields are defined at each site as $\psi^A_{\alpha a}(x)$, where x denotes the discrete site on the lattice, A is the flavor index, α is the Dirac spin index, and a is the colour index. Wilson preserved local gauge invariance by working directly with *gauge links*, the $SU(3)$ parallel transporters are defined on the elementary links between neighbouring sites:

$$U_{\mu ab}(x) \equiv U_{ab}(x, x + \hat{\mu}) \tag{1.9}$$

where a and b are colour indices. These link fields are related to the gluon field

$$U_\mu(x) \;=\; e^{iagA_\mu(x+\frac{\hat{\mu}}{2})}\,, \tag{1.10}$$

where the average field A_μ is defined at the midpoint of the link.

Under a local gauge transformation represented by $\Omega(x)$ at each site, the quark fields and gauge links transform as:

$$\begin{aligned}
\psi(x) &\to \Omega(x)\psi(x) \\
\overline{\psi}(x) &\to \overline{\psi}(x)\Omega^\dagger(x) \\
U_\mu(x) &\to \Omega(x)U_\mu(x)\Omega^\dagger(x+\hat{\mu}) \\
U^\dagger_\mu(x) &\to \Omega(x+\hat{\mu})U^\dagger_\mu(x)\Omega^\dagger(x)
\end{aligned} \tag{1.11}$$

This formulation allowed Wilson to form gauge-invariant expressions such as

$$\overline{\psi}(x)U_\mu(x)\psi(x+\hat{\mu})\,,$$

$$\overline{\psi}(x+\hat{\mu})U^\dagger_\mu(x)\psi(x)$$

and objects made the colour trace of loops of links. The simplest of these

loops is the plaquette, and is given by the trace of a product of links around an elementary loop on the lattice:

$$U_{\mu\nu} \equiv \mathrm{Tr}(U_\mu(x)U_\nu(x+\hat{\mu})U_\mu^\dagger(x+\nu)U_\nu^\dagger(x)), \tag{1.12}$$

and is denoted in figure 1.2.

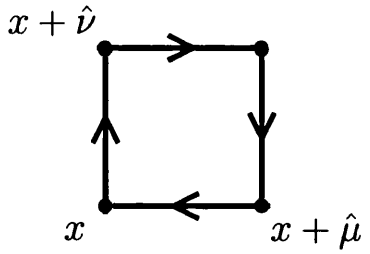

Figure 1.2: The gauge-invariant plaquette operator $U_{\mu\nu}(x)$.

The gluonic part of the action can then be constructed from these plaquettes,

$$S[U] = \sum_{Plaq} \beta \left\{ \frac{1}{N_c} \mathrm{Re}\,\mathrm{Tr}\, U \right\} \tag{1.13}$$

where $\beta = 2N_c/g^2$ with g the coupling strength. Crucially this action can be shown to coincide with the gluonic action of continuum QCD with corrections that are of order a^2.

Fermions and the Wilson term

The naïve discretisation of the fermionic term in the QCD action, i.e. replacing the derivatives with discrete differences, leads to a serious lattice artifact known as *fermion doubling* in which 15 additional massless fermion 'doublers' appear for each flavour of continuum fermion. There are many methods to improve from the naïve case, however at present there is no generic optimal choice as each type of lattice fermion also has some cost associated with it. The first method proposed, and the one used for this study, renders these doublers harmless by introducing the *Wilson term* to the action. This is an

$O(a)$ term (irrelevant in the naïve continuum limit) which gives the doublers a mass of $1/a$:

$$\begin{aligned} S_F &\rightarrow S_F - a\frac{1}{2}\sum_{x,y,\mu} a^4\psi(x)\partial_\mu\partial_\mu\psi(y) \\ &= \overline{\psi}(\sum_\mu \gamma_\mu\partial_\mu + am)\psi - \frac{1}{2}\sum_\mu \overline{\psi}\Delta_\mu\psi \\ &\equiv \overline{\psi}Q\psi \\ Q &\equiv am + \sum_\mu(\gamma_\mu\partial_\mu - \frac{1}{2}\Delta_\mu) \qquad (1.14) \\ Q_{x,y} &\equiv (am+4)\delta_{x,y} - \frac{1}{2}\sum_\mu\left[(1-\gamma_\mu)U_\mu(x)\delta_{x+\hat{\mu},y} + (1+\gamma_\mu)U_\mu^\dagger(x-\hat{\mu})\delta_{x-\hat{\mu},y}\right] \end{aligned}$$

However the cost of the addition of the Wilson term is that it explicitly breaks chiral symmetry.

A different approach to removing doublers is the application of staggered or Kogut-Susskind fermions. Here the replication is reduced from 16 to 4 flavours by assigning only a single fermion field component to each lattice site. This has much better chiral properties than the Wilson fermion and is also computationally cheaper. The number of flavours can be reduced to one by what is termed the "quarter-root trick" where the forth root is taken of the determinant, however its appropriateness is somewhat controversial [23, 24].

The Haar Measure

Another piece needed to complete the formulation of lattice QCD is to define the measure of integration over the gauge degrees of freedom. Note that, unlike the continuum fields A_μ, lattice fields are $\mathrm{SU}(N_C)$ valued matrices. Therefore, Wilson proposed an invariant group measure, the Haar measure, for this integration. This measure is defined such that for any elements V

and W of the group

$$\int dU f(U) = \int dU f(UV) = \int dU f(WU) \tag{1.15}$$

where $f(U)$ is an arbitrary function over the group. This construction avoids the problem of having to include a gauge fixing term in the path integral. This is because the field variables are compact. Hence there are no divergences and the measure can be normalised by defining

$$\int dU = 1. \tag{1.16}$$

Chemical potential on the lattice

In a non relativistic setting, the chemical potential μ corresponds to the energy 'cost' of adding an extra particle to the system. The additional term in the Hamiltonian is given by $\mu_k N_k$, where N_k is the number of particles of type k. If particle k is fermionic and the system is sufficiently dense the chemical potential will be the Fermi energy (the position of the Fermi surface). In a relativistic setting however, particles can be created and destroyed, and μ must include the rest mass of the particle. It therefore only makes sense to have a chemical potential that couples to the 0^{th} component of the relevant conserved current $J_\mu = \bar{\psi}\gamma_\mu\psi$. As expected $J_0 = \bar{\psi}\gamma_0\psi = \psi^\dagger\psi$ will then give the density of particle number, or to be more precise, the difference between the number of particles and antiparticles of type k: $\int J_0 = N_k - \bar{N}_k$.

In the continuum QCD Lagrangian, the chemical potential which couples to the quarks appears as a term μJ_0, which is equivalent to making the substitution (in Euclidean spacetime),

$$p_4 \rightarrow p_4 - i\mu \tag{1.17}$$

in the fermion propagators. However this term $\mu\bar{\psi}\gamma_0\psi$ cannot be naïvely discretised for lattice calculations as it leads to divergences in the free quark energy [25]. Instead it must be treated as an external field that couples to

the time-like components of the quark fields.

On the lattice, a free propagator of Wilson fermions can be written as,

$$\frac{1}{1-\kappa\sum_{\mu=1}^{4}\{(1-\gamma_\mu)e^{ip_\mu a}+(1+\gamma_\mu)e^{-ip_\mu a}\}}, \tag{1.18}$$

and the $\bar{\psi}\partial_\mu\psi$ term leads to $\bar{\psi}e^{ip_\mu a}\psi$. Therefore, the chemical potential can be naturally included as an exponential in the fermion matrix as,

$$\begin{aligned} M_x y(\mu) = \delta_{x,y} - \kappa\sum_{i=1}^{3}\Big\{&(1-\gamma_i)U_i(x)\delta_{y,x+\hat{i}} + (1+\gamma_i)U_i^\dagger(y)\delta_{y,x-\hat{i}}\Big\} \\ -\kappa\Big\{&e^{+\mu}(1-\gamma_4)U_4(x)\delta_{y,x+\hat{4}} + e^{-\mu}(1+\gamma_4)U_4^\dagger(y)\delta_{y,x-\hat{4}}\Big\}. \end{aligned} \tag{1.19}$$

In other words, the chemical potential couples to the forward and backward time-like links as,

$$\begin{aligned} U_t(x) &\rightarrow e^{\mu}U_t(x), \\ U_t^\dagger(x) &\rightarrow e^{-\mu}U_t^\dagger(x), \end{aligned} \tag{1.20}$$

Gavai considered a more general function than $\exp(\pm\mu)$ [26], however this exponential form is the standard method and has been shown to be "perfect" within the framework of perfect actions [27]. See section 2.3 for the details of the action used for this study.

Saturation

In general for any discrete system the Pauli exclusion principle prevents arbitrarily high fermion number density to be reached. This maximal point where each site is occupied by $2N_cN_f$ quarks is termed saturation and can be thought of as a lattice artifact[2]. In a saturated system, virtual $q\bar{q}$ pairs will be highly suppressed and the system can resemble a quenched theory.

[2]This assumes a highly local action. In general the maximal saturation level is proportional to the largest time separation with non-zero coupling, hence a non-truncated perfect action would not suffer from any saturation artifacts [27]

In general these unphysical effects begin to appear before such densities are reached depending on the action under investigation [27].

Numerical Simulation

With a complete discretisation scheme, observables can be calculated by numerically performing the discrete version of the integral in equation 1.8. However because of the exponential factor, the sum will be dominated by a small subset of gauge configurations which minimise the action. Therefore to make numerical work practical, the technique of importance sampling is employed. Here the multidimensional integration space is not explored randomly but along what is termed a Markov chain. The probability of a particular gauge configuration $\{U\}$ appearing is engineered to be given by

$$P[U] \propto e^{-S_{eff}}. \tag{1.21}$$

Thus precisely the terms which contribute most to the integral will appear and in the correct frequency so that expectation values can be calculated by simple averages

$$\langle \mathcal{O} \rangle = \lim_{N \to \infty} \frac{1}{N} \sum_{i=1}^{N} \mathcal{O}[U_i]. \tag{1.22}$$

Of course once a measurement is made it needs to be confronted with reality, which in the case of lattice calculations means taking a series of limits, the principle two being the continuum limit $a \to 0$ and the infinite volume limit $V \to \infty$. So in principle one measurement involves a series of simulations at different lattice spacing, and lattice volumes.

1.4 Dense Lattice QCD

Monte Carlo methods to evaluate the partition function (1.4) break down as soon as a non-zero chemical potential for quark number is introduced, as the

quark determinant becomes complex

$$\not{D}(\mu)^\dagger = \gamma_5 \not{D}(-\mu^*)\gamma_5 \tag{1.23}$$

and therefore the Boltzmann weight used for the updating procedure is also complex. This is not solely an issue for fermions; it can be traced to the explicit breaking of time reversal symmetry by the term with $\mu \neq 0$, which in Euclidean metric corresponds to a breaking of the symmetry under $i \rightarrow -i$.

In principle the the phase of the determinant can be quenched in the updating step and replaced in the definition of the observable to be measured. For example, a purely gluonic observable $A[U]$ could be measured by

$$\langle A[U] \rangle = \frac{\langle A[U] e^{i\phi_Q} \rangle_{S_{eff}}}{\langle e^{i\phi_Q} \rangle_{S_{eff}}} \tag{1.24}$$

where the phase ϕ_Q is defined as

$$\det Q \equiv e^{i\phi_Q} |\det Q| \tag{1.25}$$

and S_{eff} is the action with $\det Q$ replaced with its modulus. Whilst this approach is mathematically sound, in general it does not work for numerical simulations. The central problem is that the phase $e^{i\phi_Q}$ suffers from very large fluctuations and so both the numerator and denominator have to rely on delicate cancellations to achieve the correct result. For anything other than very small lattices with very small chemical potentials the precision required is simply unfeasible.

A different approach, and the first attempted historically, is that of studying the fully quenched theory, $\det Q = 1$. Such an approximation is often used in lattice calculations as the reduction in computing cost is large, indeed it made early work possible. It is equivalent to decoupling sea quarks from the theory, i.e. turning off virtual quark loops. It is clear that this approach is a non-systematic approximation to the full theory as the gauge field ensemble $\{U_\mu\}$ can only respond to $\mu \neq 0$ through these quark loops. However it was

also demonstrated that such an approach also gets the fermion sector wrong, producing a transition from the vacuum to a ground state with non-zero quark density, termed onset, that scaled with the pion mass and not the lightest baryon as would be expected. This was explained, in the context of random matrix theory, by Stephanov [28] who showed that the quenched theory should be thought of as the $N_f \to 0$ limit of a theory with an addition N flavours of conjugate quark q^c. Diquarks formed by qq^c, which at $\mu = 0$ would be degenerate with the pion, would then become the lightest baryon and so create this unphysical shift of onset. It has been shown [29] that it is precisely the cancellations amongst the fluctuation phases in the quark determinant that remove this fake signal for onset in the full theory.

Note that the sign problem is not unique to lattice QCD and indeed is a well known problem in many fields where statistical mechanics are applied. For example it appears in many condensed matter physics problems. Interestingly many systems with severe sign problems have been recently solved by the application of cluster algorithms which re-sum classes of configurations within the path integral, for example [30]. Applying these techniques to QCD however is a non-trivial task, although some progress has been made using model versions [31].

1.5 Non-zero μ Methods: Dodging the Sign Problem

A range of techniques have been developed that have been applied to effectively side-step the sign problem and have used lattice QCD simulations with other parameters to infer properties of the theory at $\mu \neq 0$. In general they incur serious computational costs or introduce systematic errors that restricts their application to a small sector of the phase diagram in the high temperature, small chemical potential limit. Nevertheless this regime of $\mu/T \lesssim 1$ is directly applicable to the study of the formation of quark gluon plasma, heavy ion experiments performed at high energy colliders (RHIC,

LHC etc.) and early universe physics.

1.5.1 Multiparameter Reweighting

Multiparameter reweighting is a generalisation of an earlier technique, the Glasgow method [32], whereby the partition function is reweighted in two parameters [33]. It can be rewritten identically as

$$Z = \left\langle \frac{e^{-S_g(\beta)} \det(M(\mu))}{e^{-S_g(\beta_0)} \det(M(\mu=0))} \right\rangle_{\mu=0,\beta_0} . \tag{1.26}$$

Here the ensemble average is generated at $\mu = 0$ and a lattice gauge coupling β_0, and the reweighting factor takes us to the values μ, β of interest.

The central issue with reweighting is that of overlap. Whilst the reweighting formula is itself exact, its Monte Carlo evaluation is not, i.e. the integral is approximated by a finite number of dominant configurations. If the two ensembles are closely related, then the measured configurations will also be important in the target ensemble. However if the target state is physically different, there must be important contributions from configurations with a very small weight in the initial state. Thus the importance sampling required to make the numerical integration feasible limits the distance in phase space that reweighting is valid from a given initial state. Without comparison to results from other methods it is very difficult to observe this introduction of systematic error as the reweighting is applied.

The advantage of the multiparameter method over the original Glasgow method [32] is that the initial β can differ from the target state as well as μ in order to try to maximise overlap. An example would be to set β to the pseudo-critical coupling $\beta_0 = \beta_{crit}$ so that the obtained ensemble probes both phases and contains a wide range of configurations.

Additional difficulties are that the reweighting factor is exponentially suppressed both with volume and chemical potential (the sign problem), and that the statistical fluctuations are those of the simulated ensemble instead

of the physical one. This correlates all reweighted measurements and so makes reliable error estimation difficult.

1.5.2 Finite Density by Taylor Expansion

A different method to gain information about non-zero μ is to compute the coefficients of a Taylor series expansion of observables in powers of μ/T. Early attempts have looked at susceptibilities and the response of screening masses to chemical potential [34, 35], and more recently it has also been used to study the phase transition and its nature [36, 37].

On finite volumes the partition function $Z(m > 0, \mu, T)$ is an analytic function of the parameters of the theory, and therefore for small enough μ/T the first few terms of a Taylor series may give an accurate description of the quantity of interest. The coefficients of these terms can be calculated at $\mu = 0$ with orthodox techniques. Moreover the partition function is even in μ because of the CP symmetry of the QCD action $Z(\mu) = Z(-\mu)$, and therefore physical observables have series expansions in $(\mu/T)^2$. However the computing the coefficients becomes increasingly difficult as the order of the terms increase.

1.5.3 QCD at Imaginary μ

In contrast to introducing a real chemical potential, there is no barrier to performing simulations with an imaginary one $\mu = i\mu_i$, as equation 1.23 shows that the quark determinant remains real and positive. The natural question is then how to translate the obtained results into information about the system at real μ.

The general method employed is to fit the imaginary chemical potential data with a truncated Taylor series in μ_i/T, and analytically continue the coefficients back to real μ. This technique was first used for observables like the chiral condensate and screening masses in the deconfined phase [38]. It was

then shown to be applicable to the phase transition itself [39], which has recently been exploited in a growing number of works [40, 41].

For complex $\mu = \mu_r + i\mu_i$, it has been shown that the QCD partition function (equation 1.4) is periodic in the imaginary direction, with period $2\pi/N_c$ for N_c colours [42], i.e. $Z(\mu_r/T, \mu_i/T) = Z(\mu_r/T, \mu_i/T + 2\pi/N_c)$. This symmetry implies that a shift in μ_i of a critical amount is equivalent to a transformation by the $Z(3)$ centre of the gauge group. This periodicity in the imaginary chemical potential plane puts a limit on the radius of convergence for the analytic continuation, which is given by the width of a sector $\mu/T = \pi/3$. Hence the approach is limited to $|\mu/T| \lesssim 1$. It is however computationally simple, much cheaper than reweighting or computing coefficients of the Taylor expansion and a good testing ground for effective QCD models. Another advantage is that its systematic errors are visible in the convergence of the fit.

1.5.4 Canonical Ensemble Method

An imaginary chemical potential is also employed in the canonical approach [43]. Here the grand canonical partition function is calculated for μ_i and can then be related to the canonical ensemble at a fixed quark number Q via an integral transform

$$Z_C(T, B = 3Q) = \frac{1}{2\pi} \int_{-\pi}^{\pi} d\left(\frac{\mu_i}{T}\right) \exp\left(-i\mu_i Q/T\right) Z(\mu = i\mu_i, T, V). \quad (1.27)$$

This Fourier transform is performed numerically. The sign problem appears in oscillations of the exponential and so the approach will only work for moderate Q and small volumes. However, this approach has no overlap problem and has been applied to study the confinement/deconfinement transition at finite μ [44].

1.5.5 An Overview and a New Approach

The canonical approach does not truly belong in the high temperature class, since its natural home will be a low temperature, small Q regime. All of the other methods are only reliable below $\mu/T \sim 1$ and so can only probe a small part of the QCD phase diagram. However they are independent and so results can be verified by cross-checking between techniques.

An additional technique that has been recently revived is that of Stochastic Quantisation [45], whereby expectation values are obtained as equilibrium values of a stochastic process. The system evolves in a fictitious time direction θ according to complex Langevin dynamics and at some later θ it converges to the correct equilibrium distribution. Such techniques are not yet fully developed or tested for full QCD, but have great potential as they appear not to be limited to small μ or by the severity of the sign problem.

Chapter 2

2-Colour QCD

2.1 Introduction to 2-Colour Quantum Chromodynamics

As previously explained, the sign problem currently prevents the use of orthodox lattice techniques to study the non-perturbative aspects of low temperature QCD at non-zero μ. An example of a QCD-like theory, which does not suffer from such problems is that of QCD with a SU(2) gauge group [46]. The gauge group has the crucial property that the in the fundamental representation fermions lie in a pseudo-real representation, which ensures that the determinant of the Dirac operator is real. Therefore with an even number of degenerate quark flavours it is positive definite and importance sampling is possible. It is the simplest gauge theory for which this is true, and so provides a useful model to study the non-perturbative effects of a chemical potential.

The pseudo-reality of 2cQCD can be expressed as an anti-unitary symmetry of the Dirac operator $\mathcal{D} = \gamma_\nu D_\nu + m$,

$$[\mathcal{D}, \tau_2 C\gamma_5 K] = 0 \quad \text{or} \quad \mathcal{D}\tau_2 C\gamma_5 = \tau_2 C\gamma_5 \mathcal{D}^*, \tag{2.1}$$

where τ_2 is the colour symmetry generator, C is the charge conjugation matrix and K is the complex conjugation operator [1]. This symmetry persists for $\mu \neq 0$ [47].

In the chiral limit ($m = 0$) the fermionic part of the 2cQCD Lagrangian in Euclidean space is given by

$$\sum_{i=1}^{N_f} \quad \bar{\psi}_i \left(\partial_\mu \gamma_\mu + igA^a_\mu \tau^a \gamma_\mu\right) \psi_i \ , \tag{2.2}$$

where $\psi_i(x)$ is a quark field of flavour i and τ^a are the generators of the $SU(2)$ colour group (the Pauli matrices). As with full QCD, in the chiral limit the Lagrangian clearly exhibits an $\mathrm{U}(N_f)_L \times \mathrm{U}(N_f)_R$ symmetry. However it can be rewritten as

$$\sum_{i=1}^{N_f} \quad \frac{1}{2}\, \bar{\psi}_i \left(\partial_\mu \gamma_\mu + igA^a_\mu \tau^a \gamma_\mu\right) \psi_i \ - \frac{1}{2}\, \psi_i^T \left(\overleftarrow{-\partial}_\mu \gamma_\mu^T + igA^a_\mu \tau^{a\,T} \gamma_\mu^T\right) \bar{\psi}_i^T \tag{2.3}$$

where it has been split into two terms and the second of which has been transposed. The overall minus sign has come from commuting the Grassmann valued fermion fields. The procedure is then to make the "operator" between the fermion fields in the transposed term the same as in the first. By integrating by parts and dropping the surface term the direction of the ∂ can be reversed, and by using

$$C\gamma_\mu C^{-1} = -\gamma_\mu^T \quad \text{and} \quad \tau_2 \tau^a \tau_2 = -\tau^{a\,T} \ , \tag{2.4}$$

the transposes on the gamma matrices and the τ^a can be replaced. Note that there is no such τ identity in QCD. Finally by multiplying through by $\gamma_5\gamma_5$ the overall sign can be flipped resulting in

$$\sum_{i=1}^{N_f} \quad \frac{1}{2}\, \bar{\psi}_i \left(\partial_\mu \gamma_\mu + igA^a_\mu \tau^a \gamma_\mu\right) \psi_i + \frac{1}{2}\, \psi_i^T C\tau_2\gamma_5 \left(\partial_\mu \gamma_\mu + igA^a_\mu \tau^a \gamma_\mu\right) \tau_2\gamma_5 C^{-1} \bar{\psi}_i^T \tag{2.5}$$

The two terms can now be combined by combining the quark fields into 2

component spinors of dimension $2N_f$.

$$\sum_{i=1}^{N_f} \frac{1}{2} \left(\bar{\psi}_i\,,\ \psi^T C\tau_2\gamma_5\right) \left(\partial_\mu\gamma_\mu + igA^a_\mu\tau^a\gamma_\mu\right) \begin{pmatrix} \psi_i \\ \tau_2\gamma_5 C^{-1}\bar{\psi}_i^T \end{pmatrix} \tag{2.6}$$

It is clear that the Lagrangian exhibits an enlarged symmetry of $\mathrm{U}(2N_f)$, which will includes transformations that link quarks and antiquarks unlike in normal QCD. This is sometimes referred to as the the Pauli–Gürsey symmetry. As with QCD the axial $\mathrm{U}(1)_A$ subgroup is broken in the quantum theory by the axial anomaly. In 2cQCD it preserves $\mathrm{SU}(2N_f)$ transformations and a vector-like $\mathrm{U}(1)_B$ symmetry which corresponds to baryon charge conservation.

In QCD chiral symmetry is spontaneously broken by the formation of a chiral condensate, with the resultant group structure $\mathrm{SU}(N_f)_L \times \mathrm{SU}(N_f)_R \rightarrow \mathrm{SU}(N_f)_V$. For 2cQCD the pattern of breaking is $\mathrm{SU}(2N_f) \rightarrow \mathrm{Sp}(2N_f)$, and as with QCD the $\mathrm{U}(1)_B$ survives. The resultant number of massless Goldstone bosons can be calculated by counting the number of broken generators. For QCD each $\mathrm{SU}(N_f)$ contains $N_f^2 - 1$ generators, and so there will be $N_f^2 - 1$ Goldstones as a result of the spontaneous chiral symmetry breaking. With $N_f = 2$ this gives 3 massless bosons, which are identified as the pions. In 2cQCD the $\mathrm{SU}(2N_f)$ gives $(2N_f)^2 - 1$ generators and the $\mathrm{Sp}(2N_f)$ contains $2N_f(2N_f + 1)/2$. This results in $N_f(2N_f - 1) - 1$ broken generators and so for $N_f = 2$ there will be 5 Goldstone bosons; the three pions as in QCD and a qq diquark and $\bar{q}\bar{q}$ antidiquark. This degeneracy will be preserved for $m \neq 0$ as the mass term has the same form as the chiral condensate, in the same way that the pions remain degenerate in QCD. The introduction of a chemical potential however will clearly break this degeneracy as it couples to the states with non-zero baryon number. The pattern of global symmetries for chirally broken 2cQCD with $\mu \neq 0$ is $\mathrm{SU}(N_f)_V \times \mathrm{U}(1)_B$. A detailed study of the symmetries of 2cQCD and its Goldstone modes is performed in [1].

The $\mathrm{Sp}(2N_f)$ symmetry, arises because the quarks and anti-quarks live in equivalent representations of the colour group. One important consequence

is that diquarks can be colour singlets and so make up the baryonic degrees of freedom of the theory. It is clear therefore that the particle spectrum of 2cQCD must be very different to full SU(3) QCD. For example, as stated in the above paragraph, the chiral multiplet contains both mesons and baryons and at $\mu = 0$ they will be degenerate[1]. In the gluonic sector however, the differences between SU(2) and SU(3) are expected to be less important. Therefore 2cQCD is a useful laboratory to study gluodynamics at a finite chemical potential, especially the issue of deconfinement at high density.

2.1.1 The Phase Diagram

The simplest scenario for QCD with a non-zero chemical potential predicts that observables such as the chiral condensate $\langle \bar{q}q \rangle$ and the quark number density n remain constant until $\mu_0 \sim m_{lb}/N_c$, where m_{lb} is the lightest baryon in the spectrum. At this point, termed onset, the system corresponds to nuclear matter as a non-zero density of quarks is induced into the ground state. A second transition at some some higher μ_c could occur where chiral symmetry is restored, and the system is that of quark matter. The following details how this general picture applies to low temperature 2cQCD. See Fig. 2.1.1. for an example of a phase diagram for 2cQCD.

Vacuum

The lightest baryon (at $\mu = 0$) in 2cQCD is a diquark and as previously mentioned is degenerate with the pion. Therefore this "vacuum" phase should extend from zero chemical potential to $\mu \sim m_\pi/2$. In the chiral limit this transition will occur at $\mu = 0$, and this along with the fact that the chiral multiplet contains baryons which couple to μ, allows the phase diagram to be studied as a function of μ within the framework of chiral perturbation theory, χPT [1]. The results of which have been successfully reproduced in

[1]The Goldstones are related by an $SU(2N_f)/Sp(N_f)$ transformation and will be orthogonal to the chiral condensate.

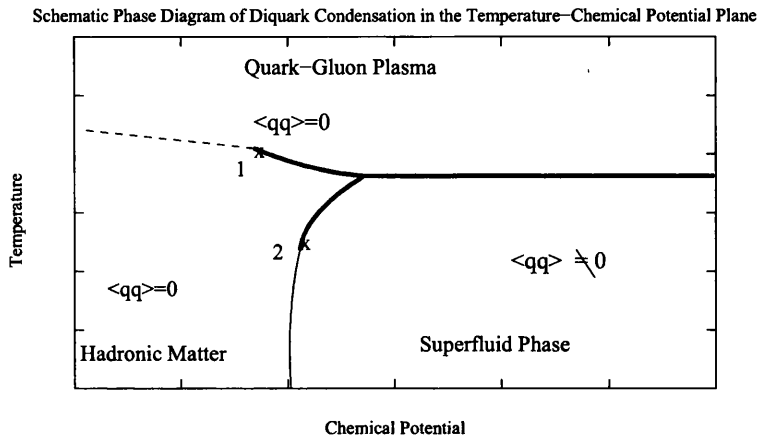

Figure 2.1: A diagram taken from [48], of a proposed phase diagram for 2 colour QCD. The dashed line is a crossover, and the solid lines are those of coexistence.

lattice studies [18]. Note that such calculations are not possible in QCD. As predicted all physical quantities in this phase remain constant with respect to μ, with the obvious exceptions being quantities that carry non-zero baryon number, e.g. baryonic observables.

Onset and the Superfluid phase

The central prediction of χPT is that a second order onset transition occurs at $\mu = \mu_0 = m_\pi/2$ to a phase with a non-zero quark density. For $N_f = 2$ the matter consists of tightly-bound scalar diquarks which Bose condense to form a gauge-invariant superfluid Bose-Einstein condensate, BEC, $\langle qq \rangle = \langle \psi^T C \gamma_5 \sigma \tau_2 \psi \rangle \neq 0$ where the matrices act on spinor, flavour and colour indices respectively. This ground state is superfluid as the non-zero baryon charge density spontaneously breaks the global $U(1)_B$ baryon number symmetry. Note that the system remains confined in this phase. This is a clear deviation from QCD, where a gauge invariant diquark operator cannot be constructed and the high density ground state is superconducting.

High density

Beyond the realm of chiral perturbation theory, at high density $\mu_c > \mu_0$, there is an expectation that system could deconfine and enter a phase analogous to the dense colour superconducting phase of full QCD. Such expectations come from NJL model studies [49] which predict a cross-over from a BEC state to a BCS superconducting state as well as hints from lattice simulations [50, 51] which found correlations between the Polyakov loop and other observables. A more detailed study of the the phase diagram of 2cQCD was subsequently carried out in [52] which found evidence for a Fermi surface and non-zero binding energy, $k_F > E_F$.

Despite also featuring a $U(1)_B$ breaking superfluid condensate, a deconfined phase would necessarily have a discontinuity in the spectrum. The confined phase consists entirely of bosonic states (mesons, diquarks, glueballs), whereas a deconfined state has squeaky excitations with half-integer spin and mass gap of the order of the non-Goldstone states. This is very different to full QCD where there is a quark/hadron continuity proposed [11]. It is clear that the study of the spectrum of 2cQCD at non-zero μ should provide information on the nature of its phase structure.

2.2 The 2-Colour Collaboration

A Swansea - Trinlat collaboration of which this work is part, is currently investigating dense 2cQCD. To be more precise, the aim is to numerically investigate the μ-axis of 2-colour QCD with 2 flavours of Wilson fermion. Wilson fermions are being used as opposed to the computationally cheaper (and more chirally symmetric) staggered fermions because the pattern of global symmetry breaking in 2-colour staggered lattice QCD is different to continuum 2cQCD [53]. This has important implications, especially concerning the particle content. For example the number of Goldstone modes will be different and the behaviour of other states will not coincide with continuum

2cQCD (see the pion prediction in figure 2.2). These differences are apparent when the Dyson index of both theories is considered: 2cQCD with fundamental Wilson quarks has $\beta_D = 1$ whereas the same theory formulated with staggered fermions in the fundamental representation has $\beta_D = 4$. This classification scheme has its origin in Random matrix theory [54] and the value of β_D is given by the number of independent degrees of freedom per matrix element and is determined by the antiunitary (time reversal) symmetries of the Dirac operator. For QCD like theories it specifies which one of the three chiral classes the given theory falls into [55].

The diagram in figure 2.2 is taken from [1] and shows the predictions of χPT for the spectrum of a range of theories. Onset occurs at 1 on the x-axis, and the pion follows the P branch and predicted to be constant in the vacuum. Post-onset in continuum 2cQCD with $N_f = 2$ (or lattice 2cQCD with Wilson fermions), the pion is predicted to follow the P_s branch and become heavier, whereas a staggered fermion is predicted to follow the P_A branch and become light for larger μ.

Additionally the presence of flavour doublers in the staggered fermion formulation causes saturation effects to occur at smaller values of the chemical potential compared to a Wilson action (see figure 3 of [27]). This can be accounted for by considering the Fermi surface of such a system. With a Wilson fermion the surface will expand in momentum space from the origin undeformed until it meets the edges of the Brillouin zone at $k_F a \simeq \pi$. With staggered fermions however there will be additional Fermi surfaces from the doublers that expand out from the opposite sides. These will intercept at $k_F a \simeq \pi/2$ and therefore saturation effects can be expected earlier. See figure 13 from [56] for an example of a Fermi surface with staggered fermions.

2.3 The 2cQCD Action

The lattice action used to generate the configurations studied within the collaboration is detailed below, with the details from [52].

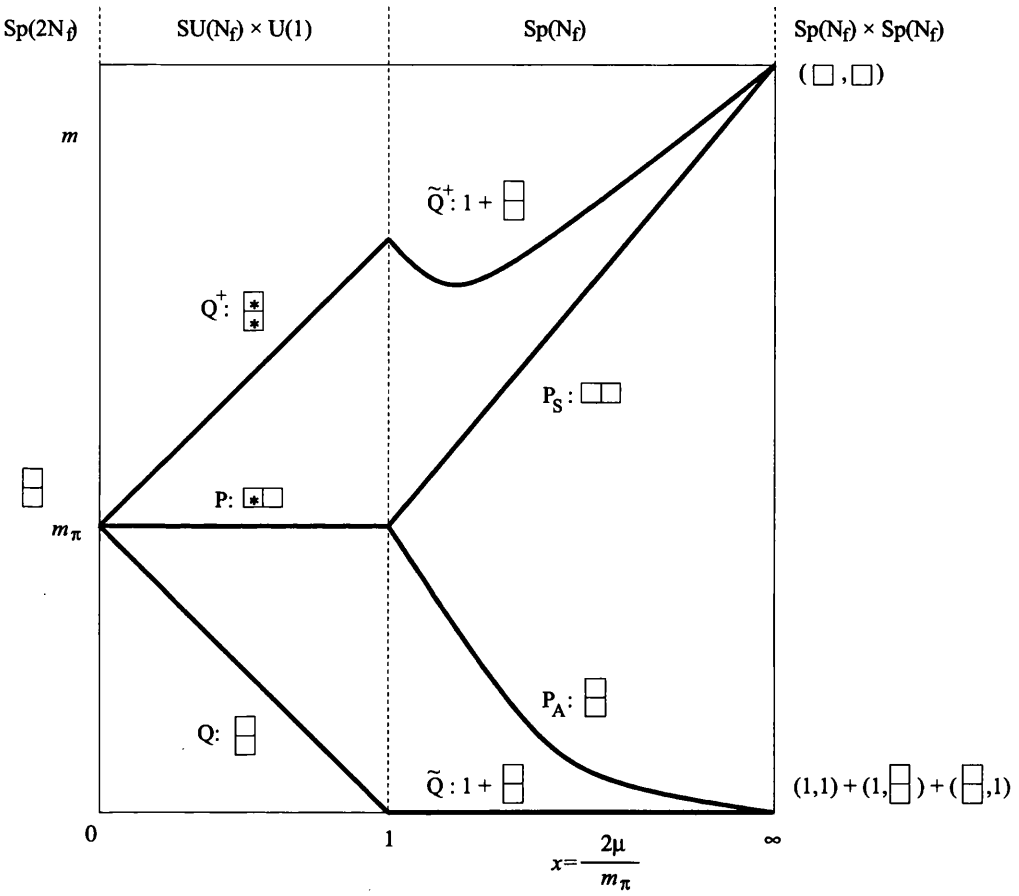

Figure 2.2: Figure taken from [1], showing the spectrum of 2-colour QCD at finite μ and m as calculated in χPT. The P branches are pion states and the Q branches describe diquarks. They are also labelled by Young's diagrams showing the multiplet structure under the corresponding residual symmetry. The star denotes the conjugate fundamental representation. The residual symmetry groups are marked above the plot. For the case of interest $N_f = 2$, the branch P_A does not exist and the degeneracies are as follows: $N_Q = N_{Q^\dagger} = 1$,and $N_{P_S} = 3$. On the left/right of the plot the residual symmetries and multiplet structure of the corresponding limiting cases $\mu = 0$ and $m = 0$ are shown.

The 2cQCD lattice action with $N_f = 2$ degenerate Wilson fermion flavours is given by

$$S = \bar{\psi}_1 M(\mu)\psi_1 + \bar{\psi}_2 M(\mu)\psi_2 - \kappa j(\bar{\psi}_1 K\bar{\psi}_2^T - \psi_2^T K\psi_1), \tag{2.7}$$

with M the conventional Wilson fermion matrix (with lattice spacing $a = 1$)

$$M_{xy}(\mu) = \delta_{xy} - \kappa \sum_\nu \left[(1-\gamma_\nu)e^{\mu\delta_{\nu 0}}U_\nu(x)\delta_{y,x+\hat{\nu}} + (1+\gamma_\nu)e^{-\mu\delta_{\nu 0}}U_\nu^\dagger(y)\delta_{y,x-\hat{\nu}}\right], \tag{2.8}$$

κ the hopping parameter, μ the quark chemical potential, and j the strength of a diquark source term.

The subscript on the fermion fields is a flavour index. The anti-unitary operator $K = K^T \equiv C\gamma_5\tau_2$, where $C\gamma_\mu C^{-1} = -\gamma_\mu^T = -\gamma_\mu^*$ and the Pauli matrix τ_2 acts on colour indices. A useful relation is

$$M^T(\mu) = -K\gamma_5 M(-\mu)K\gamma_5. \tag{2.9}$$

The fermion matrix has the following symmetries:

$$\gamma_5 M(\mu)\gamma_5 = M^\dagger(-\mu) \tag{2.10}$$

$$KM(\mu)K^{-1} = M^*(\mu) \quad \text{with} \quad K \equiv C\gamma_5\tau_2\,, \tag{2.11}$$

where the property $\tau_2 U_\mu \tau_2 = U_\mu^*$ has been used.

The last equation is the aforementioned Pauli–Gürsey symmetry which implies that $\det M(\mu)$ is real, but not necessarily positive. However, with the change of variables $\bar{\phi} = -\psi_2^{tr}C\tau_2, \phi = C^{-1}\tau_2\bar{\psi}_2^{tr}$ and defining $J = \kappa j$ the action can be rewritten as

$$S = \begin{pmatrix}\bar{\psi} & \bar{\phi}_1\end{pmatrix}\begin{pmatrix}M(\mu) & J\gamma_5 \\ -\bar{J}\gamma_5 & M(-\mu)\end{pmatrix}\begin{pmatrix}\psi \\ \phi_1\end{pmatrix} \equiv \bar{\Psi}\mathcal{M}\Psi. \tag{2.12}$$

Hence positivity of $\det\mathcal{M}$ requires the product $J\bar{J}$ to be real and positive, which translates into the requirement that the diquark source term be anti-

hermitian [57]. In fact for the simulations considered in this work J is set to be equal to $\bar{J}$.

Equation 2.12 can be used to write

$$\mathcal{M}^\dagger\mathcal{M} = \begin{pmatrix} M^\dagger(\mu)M(\mu)+|\bar{J}|^2 & \\ & M^\dagger(-\mu)M(-\mu)+|J|^2 \end{pmatrix} \tag{2.13}$$

The off-diagonal terms can be shown to vanish if $\bar{J} = J^*$ using (2.10); moreover the same identity applied to the lower block yields

$$\det \mathcal{M}^\dagger\mathcal{M} = [\det(M^\dagger(\mu)M(\mu) + \bar{J}J)]^2. \tag{2.14}$$

It is therefore possible to take the square root analytically, by using pseudofermion fields with weight $(M^\dagger M + |J|^2)^{-1}$. This has the advantage of *(a)* requiring matrix multiplications of half the dimensionality, and *(b)* permitting a Hamiltonian evaluation and hence the use of an exact HMC algorithm.

2.3.1 Physical limits and Problems with High μ

The $SU(2)_L \times SU(2)_R$-invariant diquark source term in the action is needed to regularise IR fluctuations in the superfluid phase, which appear as very small eigenvalues of the quark matrix and hugely slowdown the simulation for $\mu \neq 0$. It also allows the study of spontaneous diquark condensation on a finite system. However it is unphysical and so all observable should in theory be extrapolated to zero j.

Chapter 3

Discussion of the Applied Techniques

3.1 Spectroscopy

Masses are determined from the asymptotic properties of correlation functions in Euclidean time. A general correlator for any temperature $T = 1/\beta$ is

$$C_{ij}(t) = \mathrm{Tr}\left[O_i(t)O_j(0)e^{-\beta H}\right]/Z \tag{3.1}$$

where $Z = \mathrm{Tr}\, e^{-\beta H}$ and $O_i(t)$ are interpolating operators that act on the vacuum to create the state of interest. By rewriting

$$O_i(t) = e^{Ht}O_i e^{-Ht} \tag{3.2}$$

and inserting a complete set of energy eigenstates, (3.1) becomes

$$C_{ij}(t) = \sum_{m,n} \langle m|O_i|n\rangle \langle n|O_j|m\rangle e^{-E_n t}e^{-E_m(\beta - t)}/Z \tag{3.3}$$

Here a discrete spectrum of energy eigenstates is assumed.

At large t and low temperatures the correlation function is dominated by the

lowest states. The diagonal correlator ($i = j$) with the vacuum state "0", and the first excited "1", explicitly written out is

$$C_{ii}(t) = |\langle 0|O_i|0\rangle|^2 + |\langle 0|O_i|1\rangle|^2 \left[e^{-E_1 t} + e^{-E_1(\beta - t)}\right] + \mathcal{O}\left[e^{-E_2 t}\right] + \mathcal{O}\left[e^{-E_2(\beta - t)}\right] . \tag{3.4}$$

The first term is the vacuum disconnected term. This is generally ignored if the operator is known to have a zero vacuum expectation value, or subtracted as part of the definition of the operator. In general the operator O is an average over all the spatial sites of a given time-slice, and so projects onto states with zero momentum. E_1 is therefore the mass of the lightest state that the operator O excites. The relative size of the correction terms determine how large t must be made for the lightest state to dominate.

The asymptotic form of the diagonal correlator with $t \ll \beta$ is:

$$C_{ii}(t) \simeq |\langle 0|O_i|1\rangle|^2 e^{-E_1 t} \tag{3.5}$$

and because this is now a function of just one exponential, the mass E_1 will appear as a plateau at late time, i.e. when equation 3.5 is true in the effective mass

$$m_{eff}(t > 0) = -\ln\left[\frac{C(t)}{C(t-1)}\right] \simeq -\ln\left[\frac{e^{-E_1 t}}{e^{-E_1(t-1)}}\right] . \tag{3.6}$$

Note that this is not the only possible definition of an effective mass and whilst it is a useful visualisation tool, it provides less information than the full correlators for fitting purposes.

Fields on the lattice are subject to periodic or anti-periodic boundary conditions in time depending on whether they are bosonic or fermionic in nature. Therefore correlators in general possess terms arising from backward propagating states at large t. Indeed for meson operators this is purely a time reversed mirror-image of the state under investigation. In which case the fitted correlator will be a hyperbolic cosine of the mass and the effective mass

formula can also be changed. This can be important for fits which extend close to the centre of the lattice.

$$C_{ii}(t) = C(t) + C(N_t - t) \simeq |\langle 0|O_i|1\rangle|^2 (e^{-E_1 t} + e^{-E_1(N_t - t)}) \quad (3.7)$$

$$= 2|\langle 0|O_i|1\rangle|^2 \cosh(E_1(t + N_t/2)) \quad (3.8)$$

$$m_{eff-cosh}(t > 0) = -\cosh^{-1}\left[\frac{C(t-1) + C(t+1)}{2C(t)}\right] \quad (3.9)$$

In the case of baryon operators in full QCD the contamination comes from the state's opposite-parity partner, and will in general not have the same mass due to spontaneous chiral symmetry breaking.

3.1.1 Fermionic Correlators

In order to measure an observable that contains valence quarks, such as a meson, the interpolating operator must create or annihilate fermion fields from the vacuum. An example of such a operator is that of a current J,

$$C(t) = \sum_x \langle J(x,t) J(0,0)\rangle \,, \quad (3.10)$$

where

$$J(x,t) = \bar{\psi}(x,t)\Gamma\psi(x,t) \quad (3.11)$$

and Γ is a Dirac matrix. This is known as point-to-all correlator, as the "source" of the meson is located at a point in time and space $(0,0)$, and the "sink" is defined over an entire timeslice, t. The hadrons that the current J can create from the vacuum determine the intermediate states probed by such a correlator. The Dirac matrix Γ gives the current and thus the correlator the appropriate space-time symmetries. For example, a psuedoscalar current ($\Gamma = \gamma_5$) would couple to the pion, and a vector J ($\Gamma = \gamma_i$) would couple to

the rho. In terms of fermion fields the correlator is:

$$C(t) = \sum_x \langle 0|\bar{\psi}_i^\alpha(x,t)\Gamma_{ij}\psi_j^\alpha(x,t)\bar{\psi}_k^\beta(0,0)\Gamma_{kl}\psi_l^\beta(0,0)|0\rangle \tag{3.12}$$

where $i, j, \ldots$ subscripts label spin and α,β label colour.

The creation and annihilation operators can be contracted into quark propagators

$$\langle 0|\psi_j^\alpha(x,t)\bar{\psi}_k^\beta(0,0)|0\rangle = G_{jk}^{\alpha\beta}(x,t;0,0)\,. \tag{3.13}$$

There are two ways to combine the two $\bar{\psi}$ and ψ fields in the meson correlator: the first pairs the source ψ and $\bar{\psi}$, and therefore also the fields at the sink; and the second pairs ψ and $\bar{\psi}$ from source and sink together. The resultant correlator is

$$C(t) = \sum_x \mathrm{Tr}[G(x,t;x,t)\Gamma]\,\mathrm{Tr}[G(0,0;0,0)\Gamma] \tag{3.14}$$

$$- \sum_x \mathrm{Tr}[G(x,t;0,0)\Gamma G(0,0;x,t)\Gamma] \tag{3.15}$$

where the trace runs over the colour and spin indices. The first contraction is termed the disconnected piece, as the propagators remain separate, and is zero for a flavour non-singlet meson. Baryon correlators are constructed in the same manner, although for QCD they will of course contain three quark propagators.

3.2 All-to-All Propagators

In lattice QCD hadron spectroscopy is traditionally performed by inverting the fermion matrix with a point source. This generates fermion propagators from one point to all other points in the lattice, which are then combined with appropriate operators to produce the desired hadronic correlation functions. Whilst simple and computationally cheap, this method has a number of disadvantages, the most obvious being that it restricts the accessible physics

to the flavour non-singlet spectrum. This is because states which contain quark loops are difficult to calculate with point-to-all propagators. In addition more inversions are required for every operator that is not restricted to a point source. Finally it is clear that the construction of point-to-all propagators only uses a small fraction of the information contained within a single gauge configuration. In systems when the configuration are expensive to produce, for example in 2cQCD at high μ, an obvious priority is to extract the maximum amount of information from each one.

A solution is to use all-to-all propagators, i.e. construct the correlation function from propagators that have a source and a sink at every point on the lattice. However this is normally far too expensive to compute exactly as it requires an unreasonable number of inversions of the quark matrix. The simplest method is therefore to use a stochastic procedure to estimate the propagators. Unfortunately such methods tend to be very noisy and therefore need variance reduction methods to extract a reasonable signal.

3.2.1 Simple All-to-All Propagators

In the standard method an ensemble of random, independent noise vectors are generated, $\{\eta_{[1]}, \ldots, \eta_{[N_r]}\}$. The noise vectors run over spacetime, spin and flavour, and each entry is Z(2) or Z(4) valued. The set obeys the property:

$$\langle\langle \eta_{[r]}(X) \otimes \eta_{[r]}(Y)^\dagger \rangle\rangle = \delta_{X,Y}, \tag{3.16}$$

where $\langle\langle \ldots \rangle\rangle$ is the expectation value over the distribution of noise vectors, $\otimes$ is the matrix product between the two vectors and X, Y are labels which run over spacetime, spin and flavour. Each component of a noise vector has modulus 1. Solution vectors $\psi_{[r]}$ can then be obtained by calculating,

$$\psi_{[r]}(X) = M^{-1}\eta_{[r]}(Y)\,. \tag{3.17}$$

Writing in the spacetime, spin and flavour indices explicitly, the quark propagator from any point $x^{i\alpha}$ to any other point $y^{j\beta}$ is then given by

$$M^{-1}(y,x)^{ij}_{\alpha\beta} = \langle\langle \psi_{[r]} \otimes \eta^{\dagger}_{[r]} \rangle\rangle^{ij}_{\alpha\beta} = \lim_{N_r \to \infty} \frac{1}{N_r} \sum_{r=1}^{N_r} \psi^{i\alpha}_{[r]}(y)\, \eta^{j\beta}_{[r]}(x)^{\dagger}\,. \tag{3.18}$$

This method works but is in practise very noisy. It relies on cancellations in the noise, which is of order 1, over many samples to find the signal which in general falls off exponentially.

3.2.2 Dublin Dilution Method

This method, as proposed by the Trinlat group [58], is a modified version of the standard stochastic treatment in which the $\mathcal{O}(1)$ random noise is reduced in a systematic fashion by *dilution*. The major difference is that only a single noise vector is generated as opposed to the N_r noise vectors from the simple case. This single noise vector is then diluted with respect to some set of variables (j), $j = 0, 1, \ldots, N_j - 1$ producing N_j dilution vectors $\eta^{(j)}$ which only have support on a specific value of the variable j. The original noise vector can then be recovered by summing the complete set of dilution vectors

$$\eta(X) = \sum_{j=0}^{N_j - 1} \eta^{(j)}(X). \tag{3.19}$$

To give an explicit example, consider time dilution; in this case the noise vector η is broken up into pieces which only have support (are non-zero) on a single timeslice. That is to say, if the lattice extends for N_t steps in the temporal direction, then time dilution will produce N_t dilution vectors labelled $j = 0, 1, \ldots, N_t - 1$, such that

$$\eta^{(j)}(\vec{x}, t) = \begin{cases} \eta(\vec{x}, t) & \text{if } t = j \\ 0 & \text{if } t \neq j \end{cases} \tag{3.20}$$

Here and from now on the spin and flavour indices are suppressed. It is clear that the time diluted vectors will obey equation (3.19) and the initial noise vector is recovered by the sum of the dilution vectors.

Each diluted noise vector or dilution vector is then "inverted" by solving equation 3.17, yielding $N_d = N_t$ pairs of vectors, $\{\psi^{(j)}, \eta^{(j)}\}$, which are used to calculate an unbiased estimator of M^{-1}

$$M^{-1}(y,x) \simeq \sum_{i=0}^{N_d-1} \psi^{(i)}(\vec{x}, x_t) \otimes \eta^{(i)}(\vec{y}, y_t)^\dagger \,. \tag{3.21}$$

An Example

Take for example part of a general correlator of the form

$$C_{part} = \mathrm{Tr}(S_{ab}(y,x)\Gamma S_{cd}(w,z)\bar{\Gamma}) \tag{3.22}$$

where a, b label the propagator and encode for both the spin and flavour, and any other properties of the source and sink. Recall from equation (3.21) that a propagator S can be estimated by

$$S_{ab}(y,x) = \sum_{i=0}^{N_d-1} \psi_a^{(i)}(y) \otimes \eta_b^{(i)}(x)^\dagger \quad . \tag{3.23}$$

Each propagator can then be calculated separately by constructing an independent noise vector, diluting it and finding the solution vector. Inserting these vectors

$$C_{part} = \mathrm{Tr}(\sum_{i=0}^{N_d-1} \sum_{j=0}^{N_d-1} \psi_a^{(i)}(y)\eta_b^{(i)}(x)^\dagger \, \Gamma \, \psi_a^{(j)}(w)\eta_d^{(j)}(z)^\dagger \, \bar{\Gamma}) \quad , \tag{3.24}$$

and using the cyclicity of the trace, the correlation function can be written as

$$C_{part} = \mathrm{Tr}(\sum_{i=0}^{N_d-1}\sum_{j=0}^{N_d-1} \eta_d^{(j)}(z)^\dagger \bar{\Gamma}\psi_a^{(i)}(y)\ \eta_b^{(i)}(x)^\dagger \Gamma\psi_a^{(j)}(w)) \quad . \tag{3.25}$$

Now since the multiplications are simple dot products, the results are complex numbers and the trace is redundant.

For a time-slice correlator: $w = x, z = y$ and C_{part} is summed over all x and y, keeping a fixed t between x_τ and y_τ.

$$C_{part}(t) = \sum_{\vec{x},\vec{y},\tau}\sum_{i,j=0}^{N_d-1} \eta_d^{(j)}(\vec{y},\tau)^\dagger \bar{\Gamma}\psi_a^{(i)}(\vec{y},\tau)\ \eta_b^{(i)}(\vec{x},\tau+t)^\dagger \Gamma\psi_a^{(j)}(\vec{x},\tau+t) \tag{3.26}$$

This method is very general as any combination of the spin, flavour, colour and space components of the source vector can be used as dilution indices, and it becomes exact in the *homeopathic* limit. This is defined as where there is one diluted noise vector for each time, space, colour, flavour and spin component. Note that whilst this would require an unfeasibly large number of inversions[1] it is nevertheless a *finite* number. Therefore the path of dilution can be optimised such that the noise from the gauge fields dominate for the quantities of interest, with hopefully a small, manageable number of fermion matrix inversions.

The calculated propagator is completely general, i.e. it is a true estimation of the exact all-to-all propagator and so is independent of the operators used to construct the correlation function. Therefore if the pairs of noise and solution vectors are stored, at some later time any correlation function may be calculated for no extra inversions. The main cost then, after the propagators have been calculated once, becomes the massive file IO, i.e. the storage and processing of the large data files.

Another advantage of storing the noise and solution vectors is that if more precision is required at some later time, the dilution level can be increased

[1] This is precisely the same number as calculating the all-to-all propagator with brute force.

from N_d to N_d' diluted noise vectors with only $N_d' - N_d$ extra quark inversions. For example if $M\psi = \eta$ with $\eta = \eta^{(1)} + \eta^{(2)}$, only

$$M\psi^{(1)} = \eta^{(1)} \tag{3.27}$$

need be inverted, since $\eta^{(2)} = \eta - \eta^{(1)}$ and $\psi^{(2)} = \psi - \psi^{(1)}$.

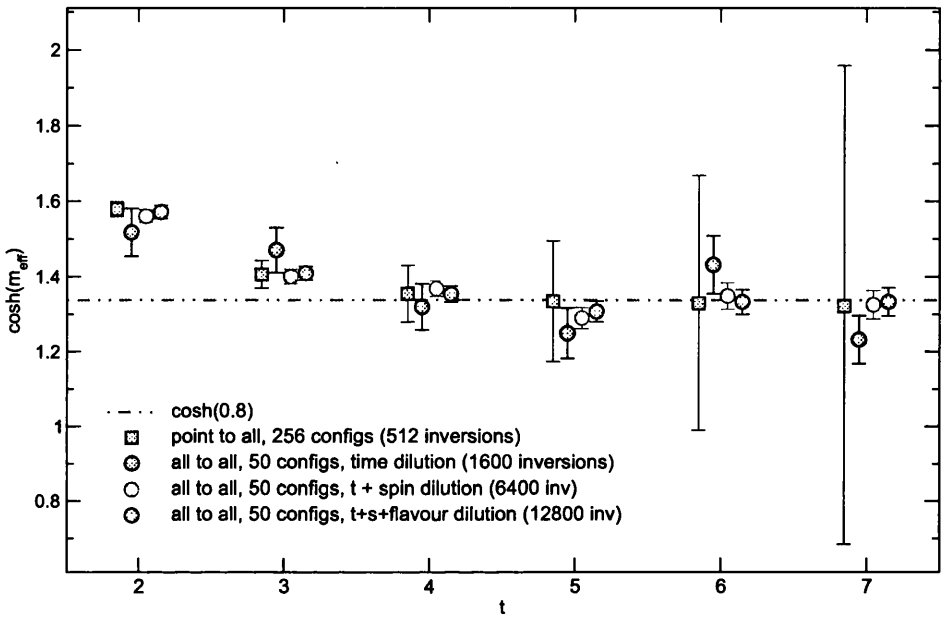

Figure 3.1: Pion effective mass plot, showing results at $\mu = 0.00$ $j = 0.00$, constructed from point to all propagators and a selection of all-to-all propagators at increasing levels of dilution. Note that the y-axis is the cosh of the effective mass, so 1 corresponds to a zero mass state. The fitted value of 0.8 is also shown.

Figure (3.1) shows a pion effective mass plot at $\mu = 0.00$ $j = 0.00$, constructed from point-to-all propagators and a selection of all-to-all propagators at increasing levels of dilution. The number of configurations and inversions used is listed in the key for each data set. Also included is the fitted value of $m_\pi = 0.80(1)$. The points have all been slightly displaced on the x-axis to aid comparison. Note that here the effective mass form used takes into account the backwards propagating state, as given by equation 3.9, and the inverse cosh has not been taken. It is clear that the all-to-all data gives a better degree of accuracy than the point-to-all despite using a fifth of the

configurations; however this plot also shows how quickly the number of inversions required for a given dilution scheme can increase. Also the all-to-all effective mass at "low" levels of dilution seems to bound or oscillate around the true value, indicating that despite the fact that the introduced noise is larger than the gauge noise, a reasonable fit is still possible.

3.2.3 So Why All-to-All for Us?

Aside from the benefits listed in the previous sections, the main advantage of Dublin all-to-all propagator for this project is that of flexibility. The simulations performed in this study are in general exploratory, therefore there is little knowledge *a priori* of the difficulty of measurement of a particular state, which states might show interesting behaviour and even what kind of operators are best suited to their measurement. This means that with this style of propagator any initial work can be reused, either to decrease the noise (by increasing the dilution), trying other operators and/or looking at other states, all with minimum cost. At least until more information is known about the particle spectrum of 2cQCD at high chemical potential, this benefit outweighs the increased cost of constructing the propagators themselves.

3.3 Glueball Techniques

3.3.1 Simple to Formulate; Hard to Measure

Whilst the purely gluonic states known as glueballs are very simple to formulate within the lattice framework, and were therefore one of the first states to be investigated, their measurement suffers from some basic problems:

- They are heavy and so require a fine lattice in the temporal direction
- The basic operators have only a small overlap with the states of interest
- The basic operators couple strongly to the ultra-violet fluctuations induced by the lattice discretisation

Over time techniques have been developed to combat these problems, with the principle advances being the use of anisotropic lattices with improved actions and using more realistic operators. By allowing a, the lattice spacing, to be finer in the temporal than the spatial directions, more data points can be obtained for a given correlator before it hits the noise floor. Such an anisotropy requires careful tuning to ensure the physics are correct, but is significantly cheaper to compute than a finer isotropic lattice. Another disadvantage is that the signals from successive time slices become strongly correlated as the anisotropy increases, however the advantages generally outweigh this issue. By taking advantage of the non-uniqueness of the LQCD action, irrelevant terms can be added to cancel lattice artifacts and improve the convergence to the continuum. Such actions are labelled "improved". For an example of a glueball study that uses all these ideas see [59].

As this work is part of an exploratory study of 2cQCD at non zero μ, the lattice action (as described in section (2.3)) is both simple and general purpose, and therefore not set up specifically for glueballs i.e. there is no temporal anisotropy. However smearing and diagonalisation techniques will be used to improve the operators, and are discussed sections 3.3.2 and 3.3.3.

The simplest glueball operators are constructed purely in terms of the plaquette $U_{ij}(\vec{x},t)$ on the ij plane and are assembled in such a way to give the operator the correct transformation properties for the state of interest. Note that the lattice explicitly breaks the full rotation symmetry to the cubic group **O**. Continuum operators can be classified by which irreducible representations of the cubic group they can be decomposed into, plus their transformation properties under parity and charge conjugation [60]. For example:

$$\phi^{0^{++}}(t) = \mathrm{Tr}\sum_{\vec{x}}\left[U_{12}(\vec{x},t) + U_{23}(\vec{x},t) + U_{13}(\vec{x},t)\right] \tag{3.28}$$

transforms in the A_1^{++} (one dimensional) representation of the cubic group and corresponds to the continuum 0^{++} scalar channel. In addition,

$$\phi_a^{2^{++}}(t) = \mathrm{Tr}\sum_{\vec{x}}\left[U_{12}(\vec{x},t) - U_{23}(\vec{x},t)\right] \tag{3.29}$$

$$\phi_b^{2^{++}}(t) = \mathrm{Tr}\sum_{\vec{x}}\left[U_{12}(\vec{x},t) + U_{23}(\vec{x},t) - 2U_{13}(\vec{x},t)\right] \tag{3.30}$$

both of which transform in the E^{++} (2-dimensional) representation and so correspond to the 2^{++} tensor channel. The lowest excitation in a channel will couple to the fundamental glueball of that symmetry, and the average over $\vec{x}$ picks out the zero momentum state. Of course these correspondences are in general not one to one, and mixing can occur with other states with the same quantum numbers. This is especially true in the superfluid phase of 2cQCD as baryon number is no longer globally conserved, however for the purposes of this study these states shall be referred to as glueball and will be labelled with their continuum names or symmetries. Masses are extracted in the standard way from the late time dependence of the timeslice correlator.

$$C_R(t) = \sum_t \overline{\phi_R}(\tau+t)\overline{\phi_R}(\tau) \tag{3.31}$$

where $\overline{\phi_R}$ is the operator ϕ_R of representation R with its ensemble-averaged expectation value subtracted from it

$$\overline{\phi_R}(t) = \phi_R(t) - \langle \phi_R \rangle \tag{3.32}$$

Note that whilst for the 2^{++} channel this vacuum subtraction is compatible with zero, it is large in the case of the scalar 0^{++} channel.

3.3.2 Building a Better Operator: Smearing

As previously outlined, simple plaquette operators have the undesired property that they couple very strongly to ultraviolet fluctuations and their overlap with the lowest lying glueball states is small. These problems only become more acute as the lattice spacing is reduced. It is clear then, that to achieve a reasonable signal both this UV contamination must be reduced and the operators be made more "realistic". A very successful method that addresses both of these points is that of smearing, whereby the simple gauge links used to construct the operators are replaced with more complicated extended objects. This has the effect of sampling the gauge fields over a larger volume, and acts to decouple unphysical modes.

The first smearing method was introduced by the APE collaboration [61]. Here links $U(x)$ are "fattened" by adding the staples that surround them with a certain weight λ. It is clear that the sum of gauge valued objects, like for example these staples, are in general no longer within the group. So there is a projection step to resolve this. This process can then be iterated N_S times to give the desired level of smearing. For example if i, j are the spatial directions then

$$U'_j(x) = \mathcal{P}_{\mathcal{G}} \left\{ U_j(x) + \lambda \sum_{\pm(k \neq j)} U_k(x) U_j(x + \hat{k}) U_k^{\dagger}(x + \hat{j}) \right\} \tag{3.33}$$

describes one iteration of spatial APE smearing, where $\mathcal{P}_{\mathcal{G}}$ is the projection

back onto the group. In SU(3) this is not a trivial step and there is no unique method, however the properties of the SU(2) group mean that this is just a matter of normalising the resultant field, $\mathcal{P}_{\mathcal{G}=\mathrm{SU}(2)}(U) = U/det(U)$. Note that here λ is outside of the sum over the spatial staples and so the smearing is isotropic in these directions, but if required more complicated smearing behaviour can be constructed. For the construction of correlation functions it is important that only the spatial terms are smeared, as this it enables the definition of the transfer matrix for the operators.

The transfer matrix T, is defined as the operator which transports a wave function at a fixed time t to $t+1$,

$$|\psi_{t+1}\rangle = \mathrm{T}\,|\psi_t\rangle\,. \tag{3.34}$$

and it is intrinsically linked to the lattice Hamiltonian $\mathrm{T} = e^{-Ha}$ and the partition function $Z = \mathrm{Tr}(\mathrm{T}^{N_t})$, and so needs to be well defined for the spectroscopy arguments of section 3.1 to hold.

Smearing technology has developed significantly since its introduction, and there are many different approaches. For example the advent of fully differential "stout" smearing [62] allowed its use within dynamical quark actions. However for the construction of improved glueball operators within this project only the basic APE smearing has been used.

The values of the two parameters N_s and λ which define a level of smearing, need to be chosen in such a way to maximise the signal. However it is not clear which values are appropriate, as heavy smearing will undoubtedly remove high energy physics. One general observation [63], is that if neither of the two parameters are too large, then it is only their product that is important, $T_s = N_s \times \lambda$. Such behaviour is evident in Fig. 3.2 which shows the effects of a range of N_s and λ on the zero time correlator $C(0)$ of the 0^{++} glueball state at $\mu = 0, j = 0.04$. The effective mass for the same correlator is shown in Fig. 3.3, where a clear improvement for the plateau at $t = 2-3$ is shown.

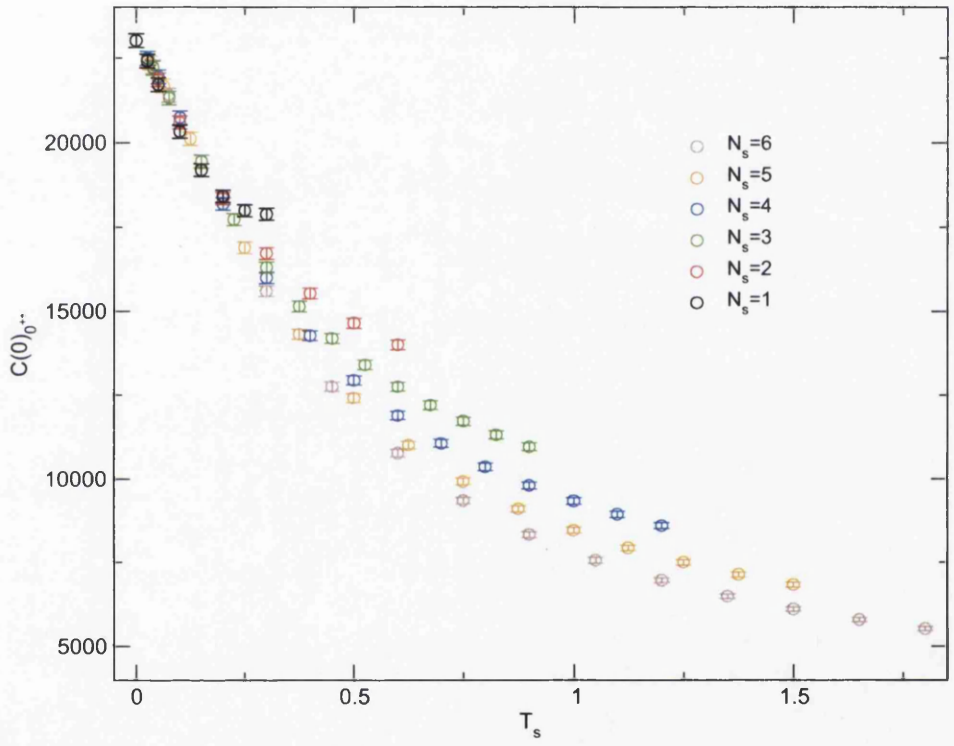

Figure 3.2: Zero time correlator $C(0)$ for the 0^{++} glueball state at $\mu = 0, j = 0.04$. Each colour is a different number of smearing iterations. The x-axis is the smearing level, T_s which is the product of the the number of iterations N_s and the smearing weight λ. The plot shows that for small $\lambda < 0.1$ the data is adequately described by just T_s.

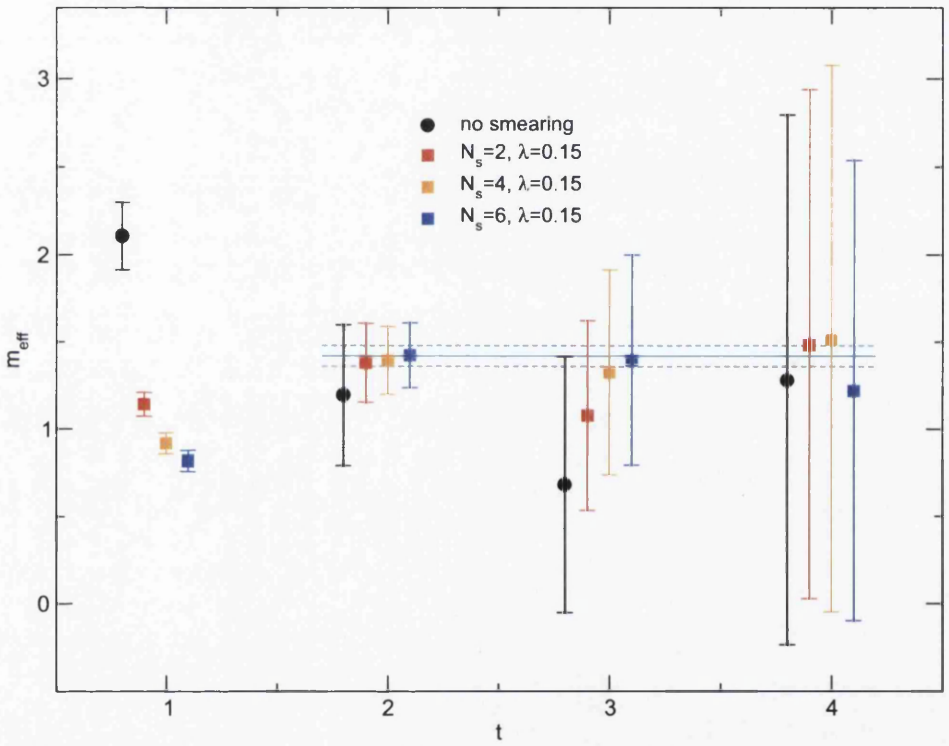

Figure 3.3: Effective mass plot for the 0^{++} glueball state at $\mu = 0, j = 0.04$, showing the effect of different levels of smearing. The fitted value of $m = 1.42 \pm 0.06$ is shown by the turquoise lines. Note that the fit was not performed to the effective mass, but rather to the diagonalised correlator directly (see chapter 5).

3.3.3 Optimal Operator Choice

For the 2^{++} channel there were already 2 simple plaquette operators with the correct quantum numbers, and now it is clear that a wide spectrum of smearing values can be applied. Since each level of smearing in effect creates a different operator, there will be a wealth of different operators to choose from. The variation principle states that,by definition the ground state of a theory is that with the lowest energy, therefore an approximation to the ground state will give a larger energy, and any reduction in its energy is an improvement in its level of approximation. So by this principle, the "best" operator will that which has the lowest effective mass for small t. This will couple least to excited states and unphysical UV contamination and most to the ground state. Now of course there is no reason to choose just one operator, as any linear combination will also be valid.

Following the techniques outlined in [64], a generalised effective mass at time t_D can be defined as

$$\tilde{m}_{eff}(t_D) = -\frac{1}{t_D} \ln \left[\frac{\sum_{\alpha\beta} v_\alpha v_\beta \tilde{C}_{\alpha\beta}(t_D)}{\sum_{\alpha\beta} v_\alpha v_\beta \tilde{C}_{\alpha\beta}(0)} \right] \tag{3.35}$$

where $\tilde{C}_{\alpha\beta}(t)$ is the correlation function between operator $\overline{\phi_\alpha}$ and $\overline{\phi_\beta}$ defined in the normal way

$$\tilde{C}_{\alpha\beta}(t) = \frac{1}{N_t} \sum_\tau \left\langle 0 \left| \overline{\phi_\alpha}(\tau + t) \overline{\phi_\beta}(\tau) \right| 0 \right\rangle \quad . \tag{3.36}$$

Let $\mathbf{v}$ denote a column vector whose elements are the optimal coefficients v_α, i.e. that would create the optimal operator. Then requiring $d\tilde{m}(t_D)/dv_\alpha = 0$ for all α leads to a generalised eigenvalue equation

$$\tilde{C}(t_D)\mathbf{v} = e^{-\tilde{m}(t_D)} \tilde{C}(0)\mathbf{v} \quad . \tag{3.37}$$

The eigenvector solution $\mathbf{v_0}$ corresponding to the largest eigenvalue $e^{-\tilde{m}(t_D)}$

then yields the coefficients $v_{0\alpha}$ for the operator Φ_0 which minimises the effective mass at time t_D as defined by equation 3.35. Assuming the correlators are well-behaved this offers the best overlap to the lowest lying state in the channel. Even if the basis (number of operators) is small, the variational principle guarantees that this is the best solution for that input.

Such techniques are very useful for looking at excited states in lattice QCD spectroscopy [65], as the next largest eigenvalue corresponds to a combination of the basis operators that is orthogonal to the first solution and also has minimised energy. Thus with an adequate basis it will couple purely to the first excited state. This is analogous to the Rayleigh-Ritz procedure in wave mechanics.

3.4 Numerical Techniques

Error analysis is an essential part of any numerical or experimental project. This is hard to overstate because it is crucial in establishing the significance of results. Jackknife errors and the consequences and measurement of autocorrelation are detailed in the following two sections.

3.4.1 Jackknife Error Estimation

Jacknife errors are generally regarded as the most appropriate method for error calculation, for the simple reason that they give the same results as the standard approach in unbiased cases and that their bias is of order $1/N$ if one is present [66]. They also eliminate the need to use error propagation formula as they are equally applicable to secondary observables (functions of measurements).

This section follows the arguments in [67]. Given a data set

$$x_i, \quad (i = 1, \ldots, N) \tag{3.38}$$

which is uncorrelated ($\langle x_i x_j \rangle = 0$ for $i \neq j$) and corresponds to a random variable x. The standard estimator $\bar{x}$, of the unknown true expectation value $\hat{x}$, is given by

$$\bar{x} = \frac{1}{N} \sum_{i=1}^{N} x_i \,, \tag{3.39}$$

and it is conventional to estimate the likelihood that $\hat{x}$ lies close to the measured $\bar{x}$ as

$$\hat{x} = \bar{x} \pm \Delta\bar{x} \tag{3.40}$$

assuming Gaussian distributions. However bias problems can appear when the expectation value of a non-linear function of $\hat{x}$ is required $\hat{f} = f(\hat{x})$. A bad estimator of $\hat{f}$ is

$$\bar{f}_{bad} = \frac{1}{N} \sum_{i=1}^{N} f_i \quad \text{where } f_i = f(x_i) \tag{3.41}$$

i.e. it will never converge to the correct value

$$\text{bias}(\bar{f}_{bad}) = \hat{f} - \langle \bar{f}_{bad} \rangle = O(1) \,. \tag{3.42}$$

where the angled brackets indicate the expectation value. A better estimator of $\hat{f}$ is

$$\bar{f} = f(\bar{x}), \tag{3.43}$$

which will typically have bias of the order $1/N$. Unfortunately this has the problem that the standard method to estimate the variance $\sigma^2(\bar{f})$,

$$s^2(\bar{f}) = \frac{1}{N} s^2(f) = \frac{1}{N(N-1)} \sum_{i=1}^{N} (f_i - \bar{f})^2 = \frac{\overline{f^2} - \overline{f}^2}{N-1}, \tag{3.44}$$

is no longer appropriate because $f_i = f(x_i)$ is not a valid estimator of $\hat{f}$. A

solution is to use jackknife estimators $\bar{f}^J, f_i^J$, as defined by

$$\hat{f}^J = \frac{1}{N}\sum_{i=1}^{N} f_i^J, \quad \text{where} \quad f_i^J = f(x_i^J) \quad \text{and} \quad x_i^J = \frac{1}{N-1}\sum_{i\neq k} x_k \,. \tag{3.45}$$

The estimator for the variance $\sigma^2(\bar{f}^J)$ is

$$s_J^2(\bar{f}^J) = \frac{N-1}{N}\sum_{i=1}^{N}(f_i^J - \bar{f}^J)^2 \,. \tag{3.46}$$

For an unbiased estimator it is straightforward to show that this formula reduces to the normal variance of the mean (3.44). For example, if $f_i = x_i$ then

$$\begin{aligned}\bar{x}^J - x_k^J &= \sum_{i\neq k}\left(\frac{1}{N} - \frac{1}{N-1}\right)x_i + \frac{1}{N}x_k = -\frac{1}{N(N-1)}\sum_{i\neq k} x_i + \frac{1}{N}x_k \\ &= -\frac{1}{N-1}\bar{x} + \frac{1}{N(N-1)}x_k + \frac{1}{N}x_k = -\frac{1}{N-1}(\bar{x} - x_k)\end{aligned}$$

and therefore

$$s_J^2(\bar{x}^J) = \frac{N-1}{N}\sum_{k=1} N(\bar{x} - x_k^J)^2 = \frac{1}{N(N-1)}\sum_{k=1} N(\bar{x} - x_k)^2 = s^2(\bar{x})$$

as each f_i^J is itself a good estimator of $\hat{f}$ and any bias that appears in $\bar{f}^J$ should in general be of order $1/(N-1)$.

3.4.2 Autocorrelation and Binning

In the previous discussion it was assumed that the data samples used to estimate the expectation value were uncorrelated; that is that they were independent. However for a numerical method that uses an update step to generate a configuration from a previous one, like for example the hybrid Monte Carlo used in lattice QCD, this statement is in general not true. If

a measurement is made on a quantity A, and t is the configuration label or sweep number, then the autocorrelation in a set $\{A_n\}$ is given by:

$$\begin{aligned}(A_n A_{n+t}) &\equiv \langle A_n A_{n+t}\rangle - \langle A_n\rangle\langle A_{n+t}\rangle \\ &= \langle A_n A_{n+t}\rangle - \langle A_n\rangle^2 = \langle (A_n - \bar{A})(A_n - \bar{A})\rangle \end{aligned} \tag{3.47}$$

using $\langle A_n\rangle = \langle \bar{A}\rangle = \langle A\rangle$. The true variance of $\bar{A}$ is then

$$\begin{aligned}\sigma_{\bar{A}}^2 = \left\langle \left[\frac{1}{N}\sum_{n=1}^{N}(A_n - \langle A\rangle)\right]^2 \right\rangle &= \sum_{\tau=-N}^{N}\frac{N-|\tau|}{N^2}(A_n A_{n+1}) \\ \underrightarrow{N\to\infty}\quad (AA)\frac{2\tau_{int,A}}{N} &\simeq (\overline{A^2} - \overline{A}^2)\frac{2\tau_{int,A}}{N}\end{aligned} \tag{3.48}$$

where $\tau_{int,A}$ is the integrated autocorrelation time and is defined as

$$\tau_{int,A} \equiv \frac{1}{2}\sum_{\tau=-\infty}^{+\infty}\frac{A_n A_{n+t}}{AA}. \tag{3.49}$$

Comparing this with the standard variance formula (3.44) it is clear that the presence of autocorrelations reduce the effective number of independent measurements by a factor of $1/2\tau_{int,A}$. This can of course be of use if making the measurement A has any significant cost in computer time, e.g. a sample of approximately uncorrelated data points with the same amount of information can be obtained by only measuring A every $2\tau_{int,A}$ configurations.

Measuring this quantity on any real data set is in general very difficult; equation 3.49 will typically diverge, as the sum goes to infinity and the noise from each term will be finite. In practise it is approximated by truncating the sum at some t such that the result is (almost) independent of t. The measured autocorrelations can also in principle have a dependence on the variable measured.

A related quantity is that of the exponential autocorrelation time, τ_{exp} obtained by assuming the autocorrelation decays in the form $\sim e^{-t/\tau_{exp}}$. This is a more general measure and relates to the properties of the updating algorithm as it measures the asymptotic behaviour of the autocorrelation [68].

The left frame of figure 3.4 shows an example of autocorrelation in the 0^{++} amplitude and average spatial plaquette at $\mu = 0$ with $N_s = 4$ $\lambda = 0.15$ measured from 2400 configurations. The data sets are normalised by their variance so that autocorrelation is 1 at $t = 0$. Both drop off very rapidly and signal is lost to the noise by around $t = 7$. It is however clear that the amplitude is the less correlated of the two measurements.

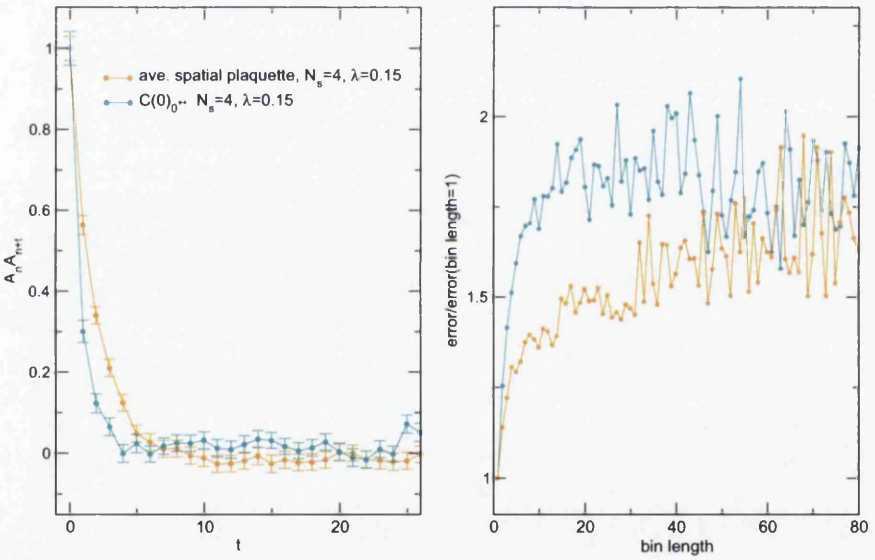

Figure 3.4: Autocorrelation (left frame) and binning errors (right) for the $N_s = 4$ $\lambda = 0.15$ 0^{++} amplitude (cyan) and spatial plaquette (orange) at $\mu = 0$.

Binning

The number of configurations required to obtain a good estimation of τ_{int} is in general unfeasible. A more practical method to take account of autocorrelations is the technique of binning the data. Here blocks of subsequent configurations are grouped, or binned, together and their measured quantities

averaged. These are then considered as independent measurements with a variance estimated by the standard formula (3.44). For this to give a correct estimate of the true variance, the bin size must be sufficiently large (larger than the autocorrelation time) that each bin is practically uncorrelated. By looking at the obtained error as a function of bin length this point can be found; below it the error should increase monotonically as the number of bins approach the number of effective independent data points, and above it the error estimate should remain constant. Of course as the bin-size increases, the number of bins will decrease, and so the obtained errors will become increasing unstable and will fluctuate. However for a reasonable data set this should occur after the bins become effectively independent, and so should not obscure this point.

Binning errors for 0^{++} amplitude and average spatial plaquette at $\mu = 0$ with $N_s = 4$ $\lambda = 0.15$ are shown in the right frame of figure 3.4. The expected plateau is visible for the amplitude data set but is less clear for the plaquette data. It is interesting to compare with the autocorrelation data for the same quantities (left frame) as the error increase measured by binning is larger for the amplitude despite it having less autocorrelations. However this assumes that the plaquette's plateau is well defined, which it does not appear to be the case.

Chapter 4

The Hadronic Spectrum

This chapter follows the published work [69] very closely and details the construction, lattice parameters, fitting and results for a selection of mesons and baryons as a function of the applied chemical potential. Additionally the Higgs and Goldstone states associated with symmetry braking in the superfluid phase are investigated and kaonic states are constructed.

4.1 Construction of Hadronic Correlators

4.1.1 Fermion Propagators

The fermion action given by equation 2.7 can be written in the form $\bar{\Psi}\mathcal{M}(\mu, j)\Psi$ where $\bar{\Psi} \equiv (\bar{\psi}_1, \psi_2^T, \bar{\psi}_2, \psi_1^T)$ and $\Psi \equiv (\psi_1, \bar{\psi}_2^T, \psi_2, \bar{\psi}_1^T)^T$. It then has the form

$$\mathcal{M} = \begin{pmatrix} A & 0 \\ 0 & \bar{A} \end{pmatrix} \quad \text{with} \quad A = \tfrac{1}{2} \begin{pmatrix} M & -\kappa j K \\ \kappa j K & -M^T \end{pmatrix}, \tag{4.1}$$

and $\bar{A}(j) = A(-j)$. The propagator is then given by

$$\left\langle \Psi(x)\bar{\Psi}(y) \right\rangle \equiv \begin{pmatrix} S_{11} & S_{12} & 0 & 0 \\ \bar{S}_{21} & \bar{S}_{22} & 0 & 0 \\ 0 & 0 & S_{22} & S_{21} \\ 0 & 0 & \bar{S}_{12} & \bar{S}_{11} \end{pmatrix} \tag{4.2}$$

where the assumption of isospin symmetry leads to the zero entries. This also implies that

$$S_{22} = S_{11} \equiv S_N; \quad \bar{S}_{11} = \bar{S}_{22} \equiv \bar{S}_N; \quad S_{21} = -S_{12} \equiv S_A; \quad \bar{S}_{12} = -\bar{S}_{21} \equiv -\bar{S}_A. \tag{4.3}$$

S_N and S_A are the normal and anomalous quark propagators. A normal propagator links two quark fields of the same flavour, whereas an anomalous one connects fields of different flavour. This, and the structure of equation (4.2) can be seen by considering isospin rotations on the two forms of propagator. A normal propagator is of the form $\psi\bar{\psi}$ and will transform under a isospin transformation as $P\psi\bar{\psi}P^\dagger$, where P is in $SU(2)$. For it to be invariant it is clear that $\psi\bar{\psi}$ must be diagonal in flavour. The anomalous propagator is structured as $\psi\psi^T$ and will rotate as $P\psi\psi^T P^T$. Using the identity $\tau_2\tau^a\tau_2 = -\tau^{a\,T}$, it can be rewritten as $P\psi\psi^T\tau_2 P^\dagger$ showing that the flavour structure must therefore be of the form τ_2 for isospin symmetry to hold.

It is important to note that at $\mu = 0$ the anomalous propagators are zero in the limit $j \to 0$ although it may not remain so in a superfluid phase due to particle-hole mixing. The combination of spacetime, spin and flavour matrices that give each operator its required quantum numbers is labelled generically as Γ.

4.1.2 Mesons

The isovector ($I = 1$) meson operators M^1 are given by $\bar{\psi}_1\Gamma\psi_2$, $\bar{\psi}_2\Gamma\psi_1$ and $(\bar{\psi}_1\Gamma\psi_1 - \bar{\psi}_2\Gamma\psi_2)/\sqrt{2}$. The charged meson correlator is then

$$\begin{aligned}\left\langle M^1(x)M^{1\dagger}(y)\right\rangle &= \left\langle \bar{\psi}_1(x)\Gamma\psi_2(x)\bar{\psi}_2(y)\bar{\Gamma}\psi_1(y)\right\rangle \\ &= -\operatorname{Tr}[S_N(y,x)\Gamma S_N(x,y)\bar{\Gamma}] + \operatorname{Tr}[\bar{S}_A(y,x)\Gamma S_A(x,y)\bar{\Gamma}^T]\end{aligned} \tag{4.4}$$

For the neutral meson correlator, the disconnected parts made up from the product of two traces cancel because of isospin symmetry. The connected parts are:

$$\begin{aligned}\left\langle M^1(x)M^{1\dagger}(y)\right\rangle &= \left\langle \bar{\psi}_1(x)\Gamma\psi_1(x)\bar{\psi}_1(y)\bar{\Gamma}\psi_1(y)\right\rangle_c - \left\langle \bar{\psi}_1(x)\Gamma\psi_1(x)\bar{\psi}_2(y)\bar{\Gamma}\psi_2(y)\right\rangle_c \\ &\quad - \left\langle \bar{\psi}_2(x)\Gamma\psi_2(x)\bar{\psi}_1(y)\bar{\Gamma}\psi_1(y)\right\rangle_c + \left\langle \bar{\psi}_2(x)\Gamma\psi_2(x)\bar{\psi}_2(y)\bar{\Gamma}\psi_2(y)\right\rangle_c \\ &= -\operatorname{Tr}[S_N(y,x)\Gamma S_N(x,y)\bar{\Gamma}] + \operatorname{Tr}[\bar{S}_A(y,x)\Gamma S_A(x,y)\bar{\Gamma}^T]\end{aligned} \tag{4.5}$$

hence the degeneracy between neutral and charged isovector mesons is manifest. The isoscalar ($I = 0$) meson $M^0 = (\bar{\psi}_1\Gamma\psi_1 + \bar{\psi}_2\Gamma\psi_2)/\sqrt{2}$ has the correlator

$$\begin{aligned}\left\langle M^0(x)M^{0\dagger}(y)\right\rangle &= 2\operatorname{Tr}[S_N(x,x)\Gamma]\operatorname{Tr}[S_N(y,y)\bar{\Gamma}] \\ &\quad - \operatorname{Tr}[S_N(y,x)\Gamma S_N(x,y)\bar{\Gamma}] - \operatorname{Tr}[\bar{S}_A(y,x)\Gamma S_A(x,y)\bar{\Gamma}^T].\end{aligned} \tag{4.6}$$

In this case there is a disconnected term, and the anomalous term has the opposite sign to that of the isovector meson. From now on the isovector 0^- and 1^- mesons will be referred to as the pion and rho respectively. Note that for $j = \mu = 0$ the difference between $I = 0$ and $I = 1$ is entirely due to disconnected diagrams, which must therefore account for the π - η' mass splitting. However for μ, $j \neq 0$ this need not be the case.

The spectrum of kaons in a dense baryonic medium has also been studied. The kaon states are modelled by isovector mesons (4.4) where one of the

quark flavours does not feel the chemical potential (see Sec. 4.2 for details of this procedure). The resulting propagator therefore approximates the behaviour of a strange quark in a medium made up from u and d quarks. Note that no attempt has been made to give the strange quarks a realistic mass; for simplicity $\kappa_s = \kappa$ has been assumed. The states studied correspond to $K^{\pm}$ ($J^P = 0^-$) and $K^{*\pm}$ ($J^P = 1^-$).

4.1.3 Diquarks

An isoscalar diquark is given by

$$D^0(x) = \frac{1}{\sqrt{2}} \left(\psi_1^T(x) K \bar{\Gamma} \psi_2(x) - \psi_2^T(x) K \bar{\Gamma} \psi_1(x) \right) \tag{4.7}$$

where K is the anti-unitary operator defined in section (2.3). This implies a diquark correlator

$$\begin{aligned} 2\langle D^{0\dagger}(x) D^0(y) \rangle = & \quad \langle \bar{\psi}_1(x) \Gamma K \bar{\psi}_2^T(x) \psi_1^T(y) K \bar{\Gamma} \psi_2(y) \rangle \\ & - \langle \bar{\psi}_1(x) \Gamma K \bar{\psi}_2^T(x) \psi_2^T(y) K \bar{\Gamma} \psi_1(y) \rangle \\ & - \langle \bar{\psi}_2(x) \Gamma K \bar{\psi}_1^T(x) \psi_1^T(y) K \bar{\Gamma} \psi_2(y) \rangle \\ & + \langle \bar{\psi}_2(x) \Gamma K \bar{\psi}_1^T(x) \psi_2^T(y) K \bar{\Gamma} \psi_1(y) \rangle \\ = & \quad 4 \operatorname{Tr}[\bar{S}_A(x,x) \Gamma K] \operatorname{Tr}[S_A(y,y) K \bar{\Gamma}] \\ & + 2 \operatorname{Tr}[S_N(y,x) \Gamma K \bar{S}_N(x,y) \bar{\Gamma}^T K] \\ & + 2 \operatorname{Tr}[S_N(y,x) \Gamma K \bar{S}_N(x,y) K \bar{\Gamma}]. \end{aligned} \tag{4.8}$$

The last two terms arising from connected diagrams cancel if $K\bar{\Gamma}^T K = \bar{\Gamma}$, which is the case for $\Gamma = i\gamma_5\gamma_j$, and add up if $K\bar{\Gamma}^T K = -\bar{\Gamma}$ implying $\Gamma \in \{\mathbb{1}, \gamma_5, \gamma_j\}$. Thus the only baryon states available in the $I = 0$ sector are 0^+, 0^- and 1^-; this is just the Pauli exclusion principle in action. The isovector diquark correlator is

$$\langle D^{1\dagger}(x) D^1(y) \rangle = \operatorname{Tr}[S_N(y,x) \Gamma K \bar{S}_N(x,y) \bar{\Gamma}^T K] - \operatorname{Tr}[S_N(y,x) \Gamma K \bar{S}_N(x,y) K \bar{\Gamma}]. \tag{4.9}$$

Here the disconnected diagrams cancel, and the connected terms only add up for $\Gamma = i\gamma_5\gamma_j$ implying $J^P = 1^+$.

Higgs and Goldstone Diquark States

The spontaneous symmetry breaking of the $\mathrm{U}(1)_B$ symmetry $\psi \mapsto e^{i\alpha}\psi$, $\bar{\psi} \mapsto \bar{\psi}e^{-i\alpha}$ in the superfluid phase [1] can be probed by studying two special diquark states in the isoscalar 0^+ sector, referred to as "Higgs" and "Goldstone" [70]. The relevant operators, which by construction yield correlation functions symmetric under Euclidean time reversal and with non-definite baryon number, are given by

$$D^{\pm}(x) = \bar{\psi}_1(x)K\bar{\psi}_2^T(x) \pm \psi_1^T(x)K\psi_2(x), \tag{4.10}$$

where the Higgs is '+' and the Goldstone '−'. After Wick contraction the correlators for the two modes are

$$\begin{aligned}\langle D^{\pm}(x)D^{\pm}(y)\rangle = {} & \mathrm{Tr}[K\bar{S}_A(x,x)]\,\mathrm{Tr}[K\bar{S}_A(y,y)] \\ & + \mathrm{Tr}[KS_A(x,x)]\,\mathrm{Tr}[KS_A(y,y)] \\ & \pm \big(\mathrm{Tr}[K\bar{S}_A(x,x)]\,\mathrm{Tr}[KS_A(y,y)] \\ & + \mathrm{Tr}[KS_A(x,x)]\,\mathrm{Tr}[K\bar{S}_A(y,y)]\big) \\ & - \big(\mathrm{Tr}[\bar{S}_A(y,x)K\bar{S}_A(x,y)K] + \mathrm{Tr}[S_A(y,x)KS_A(x,y)K]\big) \\ & \pm \big(\mathrm{Tr}[S_N(y,x)K\bar{S}_N(x,y)K] + \mathrm{Tr}[\bar{S}_N(y,x)KS_N(x,y)K]\big)\,. \end{aligned} \tag{4.11}$$

The diquark operators $D^{\pm}$, are invariant under $\mathrm{SU}(2)_L \times \mathrm{SU}(2)_R$ rotations but rotate into each other under $\mathrm{U}(1)_B$. With the choice of diquark source specified in (2.7), $\langle D^+\rangle$ is precisely the diquark condensate $\langle qq\rangle$ whose non-zero value at $j \to 0$ indicates the onset of superfluidity in the 2cQCD system.

[1] The symmetry is explicitly broken when $j \neq 0$.

If susceptibilities are defined

$$\chi_{\pm} = \sum_{x} \langle D^{\pm}(0) D^{\pm}(x) \rangle, \tag{4.12}$$

then a $U(1)_B$ Ward identity can be derived:

$$\chi_{-} = \frac{\langle D^{+} \rangle}{j} \tag{4.13}$$

analogous to the axial Ward identity for the pion propagator in QCD [70]. Assuming that the dominant contribution to χ_{-} is from a simple pole, then D^{-} couples to a mode whose mass scales with $\sqrt{j}$ and becomes massless in the limit $j \longrightarrow 0$. The Goldstone labelling is therefore appropriate. The Higgs state to which the D^{+} couples will exhibit normal scaling with j. The masses of these two isoscalar scalar diquark modes therefore probe the state of the system with respect to the $U(1)_B$ symmetry. Usefully the degeneracy between the Higgs and Goldstone is principally broken by connected diagrams formed from normal propagators (the last line of eq. (4.11)).

It is helpful to compare the superfluid phase with the similar sector in QCD, the chirally broken vacuum phase. The Goldstone then corresponds to the pions and the isoscalar scalar ($I = 0\ 0^{++}$) meson f_0 to the Higgs. In QCD these two states are distinguishable by their parity; however there are no good quantum numbers to separate them in 2cQCD at $j = 0$.

In this $I = 0\ 0^{+}$ diquark channel all three correlators will be investigated as a function of μ: the diquark, the Higgs and the Goldstone. Before onset the system is in a vacuum phase and the diquark (with definite baryon number $n_B = \pm 1$), is the physical state in this channel. The Higgs and Goldstone operators rotate into each other under $U(1)_B$ and each couple to the diquark mode. Post onset the situation is more interesting as the Higgs and Goldstone modes correspond to the physical states in the spontaneously broken groundstate, their masses should separate and scale differently with j. The diquark operator couples to them both.

4.2 Numerical Method

An ensemble of gauge configurations were generated on a $8^3 \times 16$ lattice at various values of μ using a Hybrid Monte Carlo algorithm, with the fermion action (2.7) supplemented by a standard Wilson gauge action [52]. The parameters were $\beta = 1.7$, $\kappa = 0.178$; studies of the string tension suggest a "physical" lattice spacing $a = 0.26(1)\text{fm}^2$, and studies of the $\mu = 0$ meson spectrum yield $M_\pi a = 0.79(1)$ and $M_\pi/M_\rho = 0.80(1)$ [71]. For the most part the diquark source $ja = 0.04$, however for a few values of μ the series $ja = 0.06, 0.04, 0.02$ was studied in order to permit a $j \to 0$ extrapolation. The values of μ studied are given in Table 4.1. Configurations are separated by 4 HMC trajectories of typical mean length 0.5, and are not in general independent.

μ	No. of Configurations	μ	No. of Configurations
0.00	210	0.45	281
0.10	200	0.50	248
0.25	117	0.55	410
0.30	133	0.60	441
0.35	124	0.70	382
0.40	175	0.90	159

Table 4.1: Number of configurations at each value of the chemical potential. Note that the data for $\mu = 0.90$ is in general too noisy to be of use and so is only included in a few figures.

As specified in section (3.2) the quark propagators on each configuration were calculated by all-to-all techniques using time, spin and flavour dilution. Whilst this equated to constructing $16 \times 4 \times 2 = 128$ dilution vectors per propagator and thus performing 256 inversions per configuration, this was required for acceptable statistical precision at $\mu \neq 0$. These were saved to disk and stitched into correlation functions according to the formulæ given by (4.4), (4.6). (4.8), (4.9) and (4.11). The disconnected diagrams relevant to each state were calculated and saved separately; unfortunately with the

[2]This value is based on string tension measurements on a $12^3 \times 24$ lattice and supplants those reported in [52, 71].

obtained level of statistics these contributions are both noisy and compatible with zero, hence only the connected pieces are presented.

To construct correlators for the kaonic states, partial quenching was used for the strange propagators, i.e. a further set of propagators was calculated on a $\mu \neq 0$ gauge configuration using $\mu = 0$ $j = 0.04$ valence quarks. This choice of j ensures degeneracy of states, such as K and pion, at $\mu = 0$. The two different sets of propagators were then stitched together with the relevant operators to form K and K^* states. It must be stressed that the s quark mass used was identical to that of the u/d, and clearly whilst the kaon states contain contributions from virtual u/d loops, there is no s-quark sea contribution at this stage.

To extract masses, the meson correlation functions were fitted by a cosh function. The time range was adjusted to achieve a stable fit while minimising the obtained $\chi^2/N_{\rm df}$, and the obtained mass. For $\mu \neq 0$, states with baryon number $B \neq 0$, such as the diquarks and the kaons, are no longer degenerate with their anti-particles. This results in correlators which are no longer time-symmetric and must be fitted by a sum of two independent exponentials (see fig 4.1). This can lead to problems with fitting since a four parameter fit is more susceptible to noise than one with just two.

Below onset, the states' masses naïvely receive an additive contribution $\pm\mu B N_c$. Therefore as μ increases the correlation function is increasingly dominated by the lighter of the particle-antiparticle pair, the one with $B < 0$. For $\mu > 0$ the heavier state rapidly becomes very difficult to fit.

4.3 Results

All results presented here come purely from analysis of hadron correlators formed from connected quark propagators. The result for the pion mass at $\mu = 0$ is $M_\pi a = 0.800(3)$. Chiral perturbation theory (χPT) [1], which models the weakly-interacting dilute Bose gas forming at onset, can be used

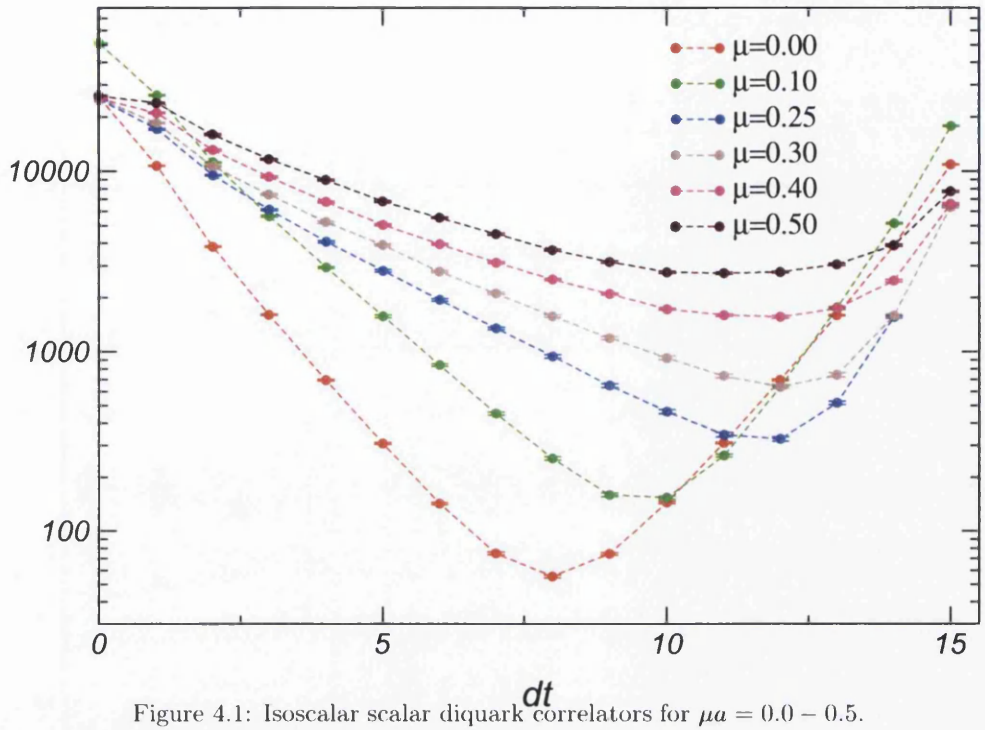

Figure 4.1: Isoscalar scalar diquark correlators for $\mu a = 0.0 - 0.5$.

to predict the onset chemical potential μ_o, where the transition from vacuum to the superfluid phase occurs. This prediction, which strictly speaking only applies when there is a separation of scales between the pion and heavier hadrons, is that $\mu_o = M_\pi/2$. This suggests that the onset in the $j \to 0$ limit should occur at $\mu_o a \simeq 0.4$. As μ is increased, it was found that more iterations are required to perform an inversion of the quark matrix [52], especially once $\mu > \mu_o$ due to the large density of small eigenvalues of $\mathcal{M}$ in the neighbourhood of the origin in this regime.

In principle all results should be extrapolated to the "physical" limit $j \to 0$, however available resources preclude a systematic study for all μ. Instead, following [52], $ja = 0.02, \ldots, 0.06$ were studied at three representative values of μ: just below onset, just above onset, and well into the superfluid phase. The results for M_π and M_ρ are shown in Fig. 4.2. Within the limits of statistical precision a linear extrapolation $j \to 0$ is valid. It is notable that the pi and rho masses have opposite slopes as functions of j, and that the

slopes change sign across the onset transition between $\mu a = 0.3$ and $\mu a = 0.5$.

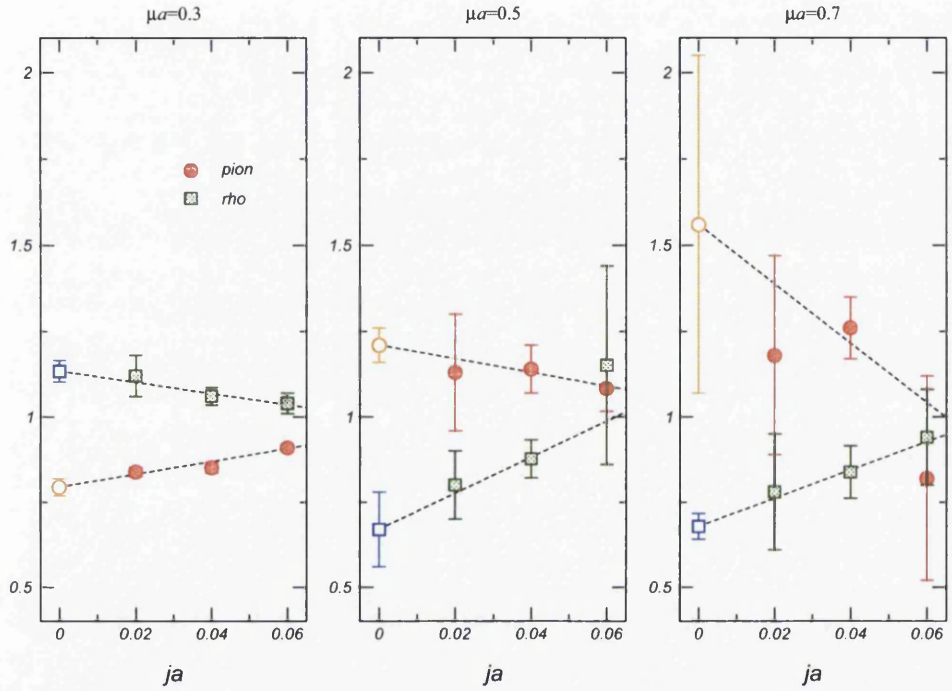

Figure 4.2: Pi and rho masses as a function of diquark source strength j for three representative values of μ, together with their values extrapolated to $j = 0$.

Results for the meson spectrum as a function of μ are displayed in Fig. 4.3. At $\mu = 0$ the isovector 0^- and 1^- states, i.e. the pion and rho, are consistent with the values found in [52, 71]. Throughout the vacuum phase ($\mu < \mu_o$) M_π and M_ρ are approximately constant as expected for states with $B = 0$, although they do show a slight increase for $\mu a > 0.2$. For the pion this appears to be a $j \neq 0$ artifact, vanishing in the $j \to 0$ limit. However things are not so clear for the noisier rho: at and beyond onset, $\mu_o a \simeq 0.4$, the pion and rho signals become much noisier as reflected in the error bars, but it is still possible to identify trends. The pion starts to become heavier at onset and appears to increase in mass monotonically with μ in the limit $j \to 0$. One can see that the χPT prediction for $j = 0$, $M_\pi = M_\pi(\mu = 0)\theta(\mu_0 - \mu) + 2\mu\theta(\mu - \mu_o)$ [1] (represented by the dotted line) is followed in a qualitative sense. The

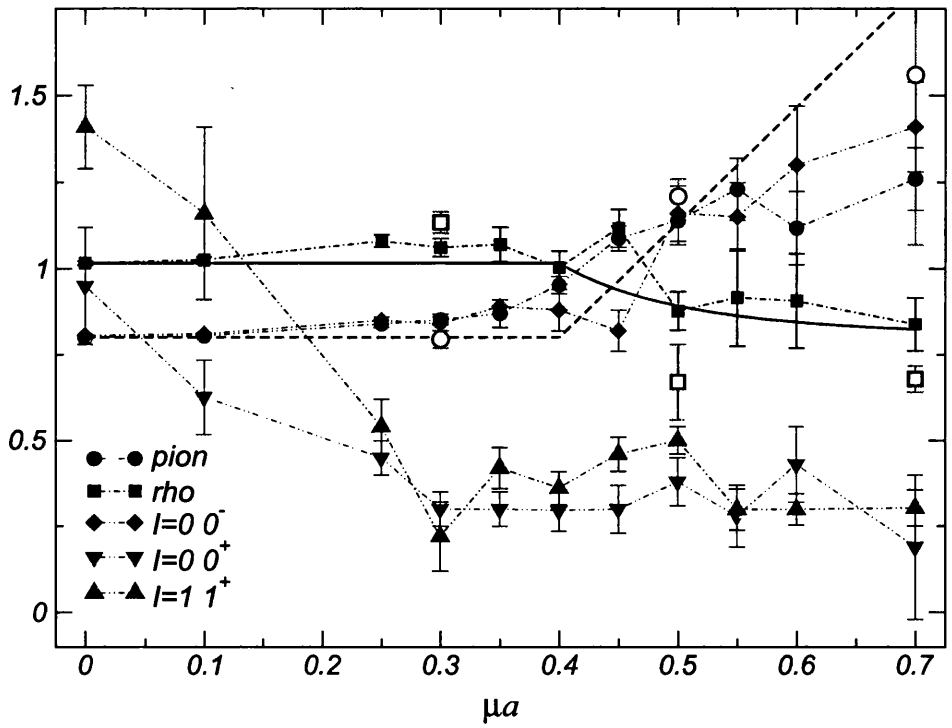

Figure 4.3: Meson masses as a function of μ for $ja = 0.04$. The dotted line is the χPT prediction for the pion and the solid line is the prediction for the rho from [72]. Open symbols denote extrapolations to $j \to 0$.

increase of the pion mass post-onset is characteristic of a state formed from q and $\bar{q}$ with a symmetric combination of quantum numbers under the residual global symmetries (i.e. the P_S state in the notation of [1]) in a theory with Dyson index[3] $\beta_D = 1$. The same trend is seen in 2cQCD simulations with staggered fermions in the *adjoint* representation [53]. However the opposite, namely a decrease in M_π post-onset, is found in a theory with $\beta_D = 4$ such as 2cQCD with fundamental staggered quarks [18].

By contrast post-onset the rho becomes significantly lighter, in agreement with the result found in simulations on $4^3 \times 8$ using significantly heavier quarks by the Hiroshima group [50]. This effect becomes stronger as $j \to 0$. Reduction of M_ρ in a nuclear medium has been proposed to explain the low mass lepton pair enhancement observed in heavy ion collisions [73]. With the exception of the point at $\mu a = 0.45$, M_ρ seems to follow the predictions of an effective model description of spin-1 excitations in 2cQCD [72]

Results for isovector 0^+ and isoscalar 1^+ states are omitted from Fig. 4.3 because the data sets are too noisy to fit, and for the isoscalar 1^- for the sake of clarity. The latter follows the rho almost exactly until $\mu a > 0.5$ at which point it becomes too noisy to measure. The results for the isoscalar 0^- are however included. Since only the connected diagrams are currently being considered, the difference between these two states and the pion and rho is just the sign of the anomalous term in (4.4, 4.6). The fact that they are the same until onset shows that this term is negligible in this regime. Beyond onset, there is a small window in which the 0^- in the isoscalar channel is significantly lighter than the isovector, and is indeed roughly degenerate with the $I = 0$, 0^- diquark of Fig. 4.5, to be discussed below.

The two remaining mesons shown in Fig. 4.3, the isovector 1^+ and isoscalar 0^+, show a similar behaviour, both starting off relatively heavy (and noisy) and then rapidly dropping as μ increases. By $\mu a = 0.3$ they have reached a minimum and stay more or less constant as μ increases further. We shall argue below that the low mass of the 0^+ state is due to its overlap with the

[3]See section 2.2 for a brief description of the Dyson index

Goldstone boson in the superfluid phase, when baryon number ceases to be a good quantum number; the low mass of the 1^+ is more unexpected.

To understand the physics of the diquark sector, it is helpful to begin with the Higgs and Goldstone states of Eq. (4.11), with a varying diquark source strength j. Fig. 4.4 shows Higgs and Goldstone masses as functions of μ at

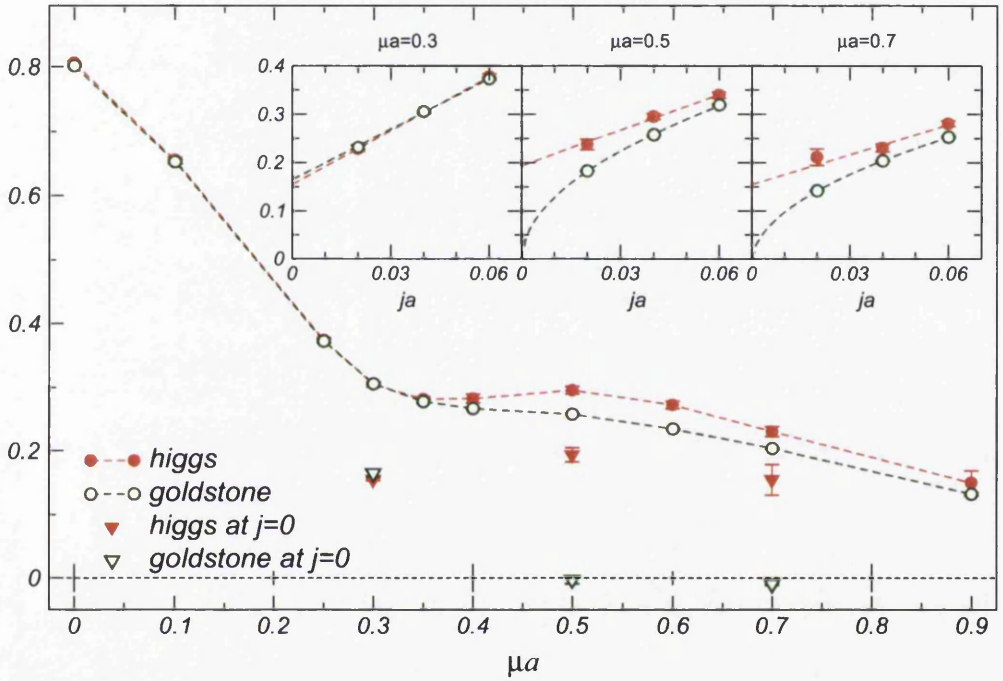

Figure 4.4: Higgs and Goldstone masses as a function of μ. The three insets show results as j is varied at fixed $\mu a = 0.3, 0.5, 0.7$. Extrapolations to $j = 0$ are displayed on the main graph with triangle symbols.

$ja = 0.04$. The insets show how the two states scale with j at the three selected values of μ. Below onset the Higgs and Goldstone are degenerate, both scaling approximately linearly with j [4]. Post-onset the degeneracy is broken, and the relation $M_{Gold} \propto \sqrt{j}$ predicted in χPT [1] appears to hold, the $\chi^2/N_{\rm df}$ being 0.67, 0.62 and 1.65 for the three linear Higgs extrapolations, and 1.08, 2.69 and 0.24 for the three Goldstone extrapolations, which have the form $M_{Gold} = a\sqrt{j} + b$ above onset.

[4]The pre-onset behaviour $M(j) = M(0)(1+bj^2)^{\frac{1}{4}}$ predicted by χPT [1] may be difficult to distinguish from linear behaviour in this regime.

Extrapolations to $j = 0$ using these scaling assumptions are also displayed on the main graph (triangular symbols). The two states remain degenerate until onset at which point the Goldstone becomes lighter than the Higgs, and appears to become massless as $j \to 0$. This is a clear manifestation of spontaneous breaking of $U(1)_B$ symmetry for $\mu > \mu_o$, implying a superfluid ground state in which baryon number is no longer a good quantum number, and therefore meson and diquark states are in principle indistinguishable.

The diquark spectrum in the remaining spin-0 and spin-1 channels is shown in Fig. 4.5. It is striking that the signal-noise ratio is much higher for some diquarks than for the mesons, a feature also seen in simulations with staggered fermions [18]. The two cleanest signals are for the isoscalar 0^+ and the isovector 1^+. The first observation is that, as a consequence of the symmetry given in equation 2.9, there is a relation between the meson and diquark spectra which holds for $\mu = j = 0$ if disconnected diagrams are neglected

$$M_D(J^P) = M_M(J^{-P}). \tag{4.14}$$

For $0 < \mu < \mu_o$, during which the physical ground state remains the vacuum, the simple prediction is that $M_D(0^+) = M_\pi \pm 2\mu$, $M_D(1^+) = M_\rho \pm 2\mu$, which is shown as dot-dashed lines in Fig. 4.5. Indeed both diquark particle-antiparticle pairs behave as expected up to $\mu a \approx 0.3$. Diquark masses are not shown beyond $\mu a = 0.25$ as the fit becomes unreliable, as explained in Sec. 4.2. After this both 0^+ and 1^+ anti-diquark states flatten off and slowly decrease with μ. The other two isoscalar diquarks constructed from local operators, namely the 0^- and 1^-, are extremely heavy and hard to fit below onset, but above onset have a sufficiently good signal for us to deduce masses comparable with $M_\pi(\mu = 0), M_\rho(\mu = 0)$.

The $I = 0$ 0^+ diquark results are overlaid on the Higgs and Goldstone data in figure 4.6. As expected there is very little difference between the masses of all three diquark operators in the vacuum phase. Post onset the diquark is noisier but appears to be at least as light as the Goldstone. This difference in noise levels is to be expected as the Higgs/Goldstone modes are time

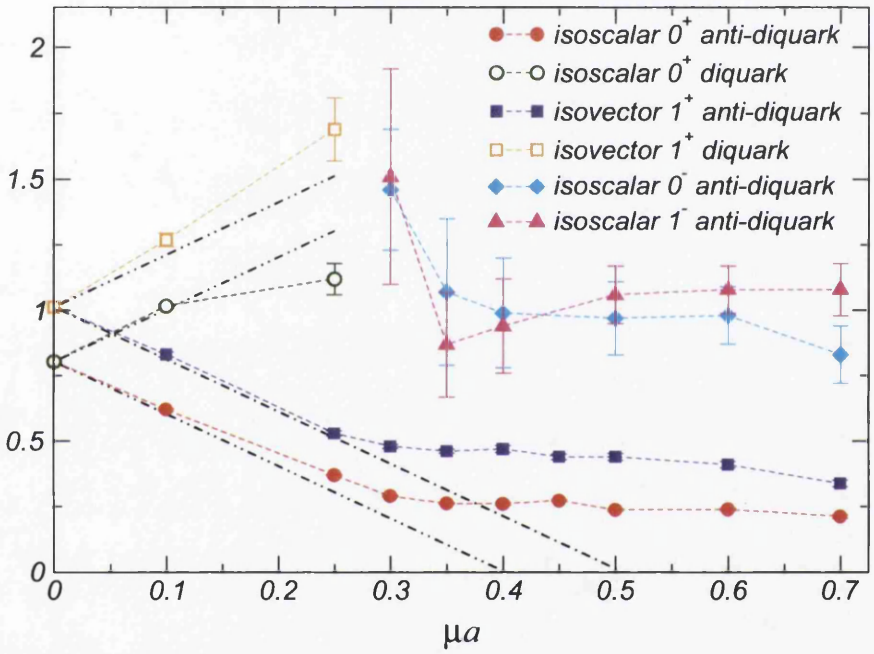

Figure 4.5: Diquark masses as a function of μ. Only states corresponding to operators with $B < 0$ are displayed for $\mu a > 0.25$. The dot-dashed lines have intercepts at $M_{\pi,\rho}$, and gradients ± 2.

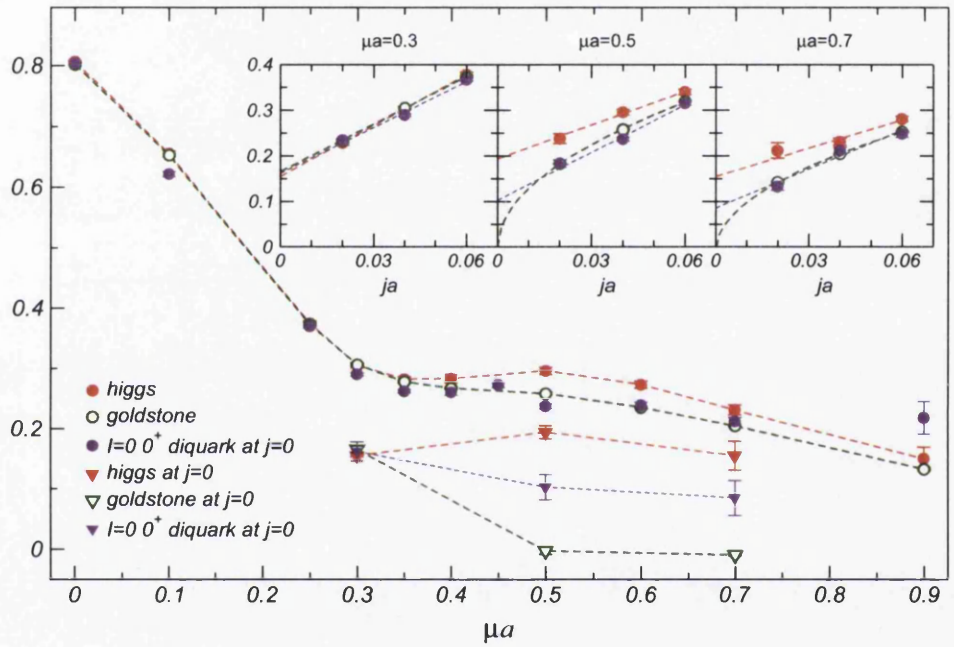

Figure 4.6: Copy of the Higgs and Goldstone graph, figure (4.4), overlaid with the isoscalar scalar diquark data. The masses at fixed $j = 0.04$ are shown as circular points in the main graph as function of μ. The three insets show results as j is varied at fixed $\mu a = 0.3, 0.5, 0.7$.

Extrapolations to $j = 0$ are displayed on the main graph with triangle symbols.

symmetric and therefore easier to fit. The j-scaling data is also presented and the linear fits shown. The choice of linear is somewhat ambiguous as the data is noisy. The resultant points lie approximately midway between the Higgs and Goldstone extrapolations. With better statistics and larger lattices it is expected that the diquark operator's coupling to the Goldstone mode would become clearer as the lightest mode in the channel should dominate the correlator at large t [5] assuming sufficient overlap. The scaling would then become more obviously $\sqrt{j}$, and so such a fit would be justified.

Although the noise in the meson sector is admittedly large, the approximate degeneracy between meson and baryon sectors in the isoscalar 0^+ and the isovector 1^+ channels is evident when the states are overlaid, as shown in Fig. 4.7. This is consistent with the meson-baryon degeneracy in the superfluid state discussed above. The noise in the isoscalar 0^- and the isoscalar 1^+ channels prevents a similar observation; however it is interesting to note that there is overlap in the crucial region $\mu = 0.4 - 0.6$. Meson-diquark degeneracy has also been observed in quenched studies at $\mu \neq 0$ with staggered fermions [74].

The isoscalar 0^- diquark is a state of interest in 2cQCD, since due to meson-baryon mixing in the superfluid phase it has the same quantum numbers as the η' meson [75]. Hence its mass acts as a probe of instanton effects and/or possible restoration of the $U(1)_A$ symmetry in a baryonic medium. Unfortunately the current simulations are not close enough to the chiral limit to settle this issue via observation of a $\pi(\mu = 0)$-$\eta'(\mu)$ mass splitting. In order to explore a more chiral system, partial quenching in κ was performed to simulate the effects of using a lighter quark mass. If indeed the diquark is being made artificially heavy then its mass would be expected to scale with the pion mass. The results are shown in figure 4.8 and the number of configurations used are recorded in table 4.2. The upper frame shows the pion mass and pion/rho mass ratio at $\mu = 0$ and the expected decrease of both of these quantities is observed as κ is increased towards κ_{crit} [6]. The

[5] See section 3.1

[6] From the partially quenched pion data $\kappa_{crit} \sim 0.192$

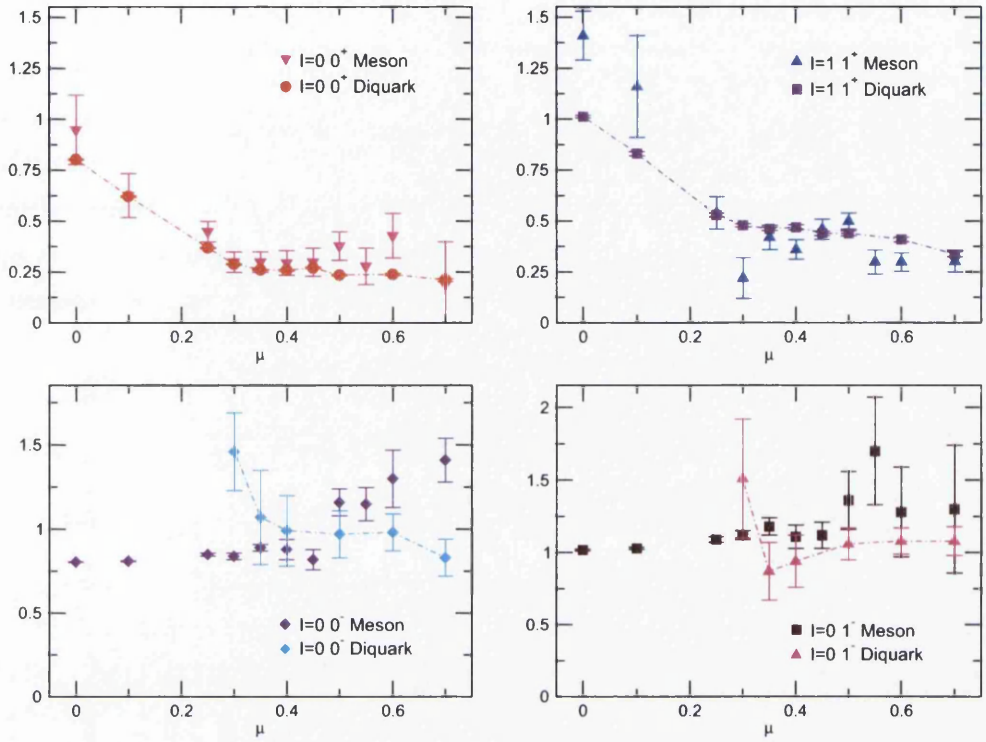

Figure 4.7: Diquark and meson masses are plotted as a function of μ, and are organised by their symmetries. Note that only the channels for which there has been observed signal in the superfluid phase for both the $q\bar{q}$ and qq state are shown. As before the $\mu < 0.3$ data for the isoscalar 0^- and the 0^+ states is not displayed. Evidence for post-onset meson-baryon degeneracy is observed in the isoscalar 0^+ and the isovector 1^+ channels (upper two panels); however the data is not sufficiently clean in the isoscalar 0^- and the isoscalar 1^+ channels (lower two panels) to make a similar observation.

No. of Configurations		
κ	$\mu = 0$	$\mu = 0.60$
0.1765	50	
0.1780	50	441
0.1795	20	300
0.1850	20	441

Table 4.2: Number of configurations used for the partial quenched data presented in figure 4.8. 20 configurations were used for the all the unlisted $\mu = 0$, κ values.

lower frame displays the pion, rho and 0^- diquark masses as a function of κ at $\mu = 0.60$. It is difficult to say whether or not the diquark scales, as the change in the measured pion mass $\sim 6\%$ over the interval $\kappa = 0.1780 - 0.185$ is small compared with the level of error in the 0^- mass, which is greater than 10% for the unquenched result. Whilst the data is not incompatible with such scaling, the precision of the both the unquenched mass measurement ($\kappa = 0.1780$) and that of the partially quenched κ would have to be greatly increased to make a conclusive statement.

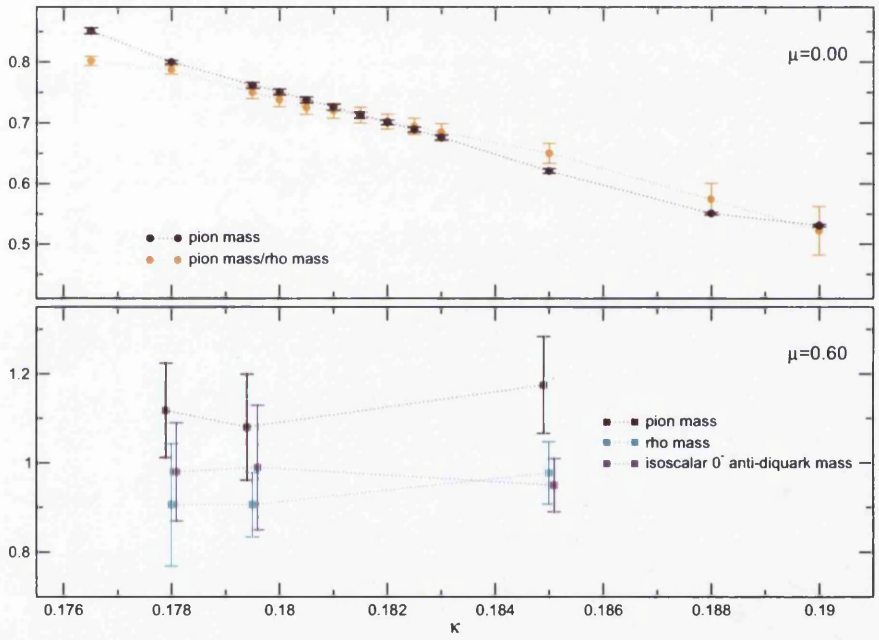

Figure 4.8: Results of partial quenching in κ on the pion mass and pion/rho mass ratio at $\mu = 0.00$ (upper frame) and the pion, rho and isoscalar psuedoscalar diquark at $\mu = 0.60$ (lower frame). Note that in the lower frame the pion and the diquark have been slightly offset in κ to aid legibility, the rho data points are at the correct κ values. The unquenched measurements are at $\kappa = 0.1780$.

The kaon spectrum is shown in Fig. 4.9. Since μ_s is assumed to be zero these states in effect carry a baryon charge conjugate to μ, and hence in general their correlators are not forwards-backwards symmetric. Some care must be taken in assigning physical quantum numbers to the states [70]. Consider say the 0^- excitation in a simple model in which the quarks are non-interacting but have mass m. Below onset the "light" quark spectrum is

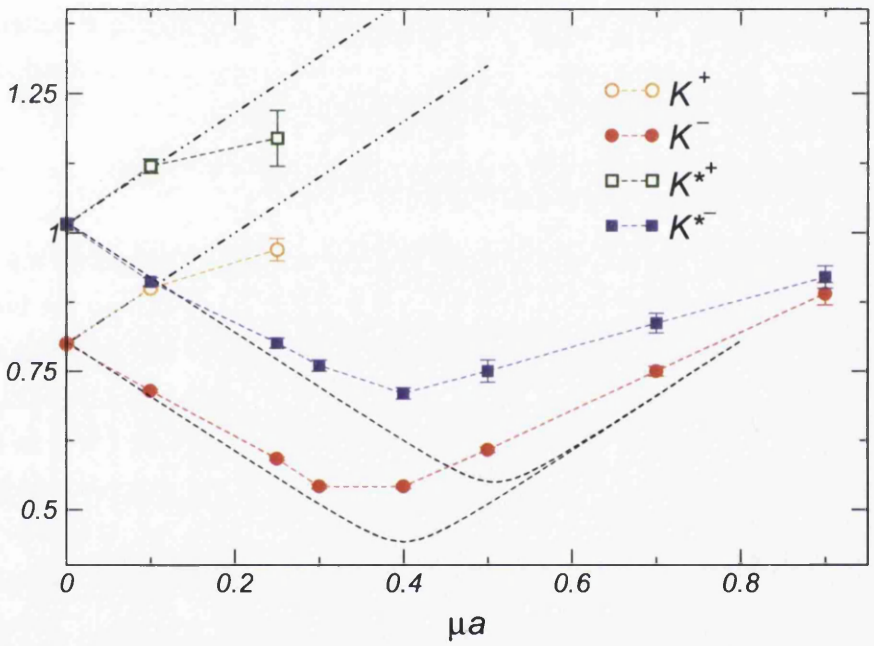

Figure 4.9: Kaon spectrum as a function of μ. Only the K^- states are displayed for $\mu a > 0.25$. Dot-dashed lines correspond to $M_K = M_{\pi,\rho}(\mu = 0) + \mu$, while the dashed line corresponds to (4.15) with $\vec{p} = \vec{0}$ and $m = M_{\pi,\rho}(\mu = 0)/2$

split into two branches, a hole branch with energy $E_h = \sqrt{p^2 + m^2} - \mu$ and a particle branch with $E_p = \sqrt{p^2 + m^2} + \mu$, while the s-quark has energy $E_s = \sqrt{p^2 + m^2}$, independent of μ. A zero momentum "K^-" state with energy $E_s + E_h = 2m - \mu$ can be identified, along with a "K^+" state with $E_s + E_p = 2m + \mu$. Above onset, the particle branch becomes filled up to some momentum $p_F = \sqrt{\mu^2 - m^2}$, so that the light quark hole state now costs energy $E_h = \mu - \sqrt{p^2 + m^2}$. The K^- state now has $E = E_s + E_h = \mu$, independent of $\vec{p}$, implying a very small in-medium velocity. If the discussion is modified to include the effect of a non-zero diquark source, then the behaviour both below and above onset is described by the single solution

$$E(\vec{p}) = \sqrt{(\mu - \sqrt{p^2 + m^2})^2 + j^2} + \sqrt{p^2 + m^2 + j^2}. \qquad (4.15)$$

Fig. 4.9 shows that this simple picture qualitatively works quite well in both K and K^* channels, even once interactions are present if we replace the vacuum mass $2m$ with the $\mu = 0$ mass of the corresponding meson from Fig. 4.3. The observed M_K always exceeds the model prediction, but appears to match both at $\mu = 0$ and $\mu \to \infty$ and retains a minimum for $\mu \approx \mu_o$. There is thus a significant range $\mu_o < \mu \lesssim M_K$ in which M_{K^-} lies below its vacuum value, and similarly for $M_{K^{*-}}$. This offers theoretical support for the idea that in-medium modification of kaon masses in nuclear matter leads to deeply-bound K^--nuclear states [76], for which there is some experimental support from scattering kaons on light nuclei [77]. Of course, simulations with realistic quark masses are needed before this observation can be taken seriously, not to mention the extension from two colours to three. Nonetheless, we can identify a minimal requirement for the existence of kaonic-nuclear bound states, namely $M_K > \mu_o$. This inequality is satisfied in QCD.

Quantum	Numbers	Meson		Diquark	
		$\mu < \mu_o$	$\mu > \mu_o$	$\mu < \mu_o$	$\mu > \mu_o$
$I = 0$	0^+	noisy	good	good	good
$I = 0$	0^-	good	noisy	noisy	good
$I = 0$	1^-	good	noisy	noisy	good
$I = 0$	1^+	no signal	no signal	-	-
$I = 1$	0^+	no signal	no signal	-	-
$I = 1$	0^-	good	noisy	-	-
$I = 1$	1^-	good	noisy	-	-
$I = 1$	1^+	noisy	good	good	good

Table 4.3: Informal summary of the success of our hadron fits. States where there are no connected diagrams are labelled by a $-$.

4.4 Discussion

The hadronic findings are summarised in a table (4.3) in which the quality of the fits both below and above onset are given. The main observations of the hadronic study are:

- The reversal of the pion and rho levels on crossing from vacuum into a baryonic medium. In the vacuum $\mu < \mu_o$ $M_{\pi,\rho}$ is approximately constant, probably because there is no diquark state with the same quantum numbers with which to mix.

- The breaking of the degeneracy between Higgs and Goldstone diquark states for $\mu > \mu_o$; the Goldstone mass scales as $\sqrt{j}$ in accordance with general theoretical properties of spontaneous symmetry breaking by condensation of fermion pairs.

- Further evidence for meson-baryon mixing in the degeneracy of $I = 0$, 0^+ and $I = 1$, 1^+ states for $\mu > \mu_o$. Post-onset the 1^+ appears to be the next lightest state after the Goldstone and Higgs. The fact that the mesons with these quantum numbers appear not to have constant mass, even pre-onset (see Fig. 4.3), can also be ascribed to meson-baryon mixing, since for $j \neq 0$ there is a non-zero amplitude for $\bar{\psi}\psi$ to project onto a baryon.

- Partially quenched kaonic states provided evidence of the possibility of bound kaons in nuclear matter as they were lighter in the superfluid phase than the vacuum.

This hadronic spectrum study has uncovered little about the effects of a second deconfining phase transition suspected to occur at $\mu_d a \approx 0.65$ in this system [52]. The only possible discernible trend is a levelling off of the already massive pion state for $\mu a \gtrsim 0.5$ seen in Fig. 4.3. However the statistical noise at high μ makes this observation provisional at best. In a deconfined phase we might expect mesons and baryons to be formed from particle-hole and particle-particle pairs in the neighbourhood of a Fermi surface, and it is possible that the local operators used in this study have a poor projection onto the true quasiparticle excitations.

Outlook

It is clear that to resolve the question of a hadronic response to a high μ change of phase then a large improvement must be made in resolving the states at mid to high chemical potential. This will no doubt involve larger statistics, probably a larger/finer temporal lattice extent and a more realistic operator. Smeared and extended operators could well help in the non-vacuum phases.

The disconnected diagrams would require some more numerical work also, but their properties and how they respond to a chemical potential would certainly be interesting. Finally some studies of a more chiral system would help to resolve the issues around the isoscalar 0^-.

Chapter 5

Glueball Studies and Results

This chapter is very much inspired by the paper by Lombardo et al. [78] which studied a very similar system and thus it will provide a clear point of comparison. They looked at the scalar glueball of 2-colour lattice simulation with two flavours of staggered fermions (eight physical flavours) at zero diquark source.

Their principal results were as follows:

- Clear difference in the smearing behaviour before and after onset.
- The measured glueball amplitude was constant in the vacuum, peaked at onset and then was much smaller post-onset.
- Post-onset the glueball was significantly lighter.

5.1 Numerical Methods

Glueball correlation functions were constructed from configurations generated by the action as described in chapter 2, using the same parameter set as the previous chapter. Table 5.1 contains the number of configurations generated at each value of μ. Glueball correlators corresponding to the scalar and

tensor states, 0^{++} and 2^{++} respectively, were constructed using the methods described in section 3.3.

μ	No. of Configurations	μ	No. of Configurations
0.00	2400	0.45	1019
0.10	1014	0.50	869
0.25	1300	0.52	845
0.30	1100	0.55	726
0.35	1001	0.60	619
0.38	954	0.70	451
0.40	935	0.90	260

Table 5.1: Number of configurations used for glueball calculations at each value of the chemical potential.

Four different types of fit were applied:

- Cosh fits over the entire interval $t = [1 : 15]$ to the basic operator.
- Cosh fits to the diagonalised correlator over an appropriate range in order to minimise the $\chi^2/d.o.f.$, which was in general $t = [1 : 4, 5]$.
- Cosh fits with an additional free parameter c over a selected interval, in general $t = [1 - 5]$.
- Cosh fits to the diagonalised correlator with an additional constant term c over a selected interval, in general $t = 1 - 5$.

All errors are calculated using the jackknife procedure, and the amplitudes are binned to take account of autocorrelations.

5.1.1 Smearing Analysis and Operator Construction

As previously discussed some form of smearing in the operator construction is essential in order to resolve glueball correlators. After analysis of a wide range of smearing weights at $\mu = 0.0$, the basic operators were constructed at 4 iterations of APE smearing, $N_s = 4$ with weight $\lambda = 0.15$. Four simple

operators were combined and diagonalised as described in section 3.3.3 to form improved or diagonalised operators. They were created from applying two sets of smearing values, $N_s = 2, 4$ $\lambda = 0.15$ to two different simple plaquette operators. The average spatial plaquette and the average 2×2 spatial plaquette were used for the scalar glueball and the two different tensor operators as detailed in equation (3.29) for the 2^{++} state.

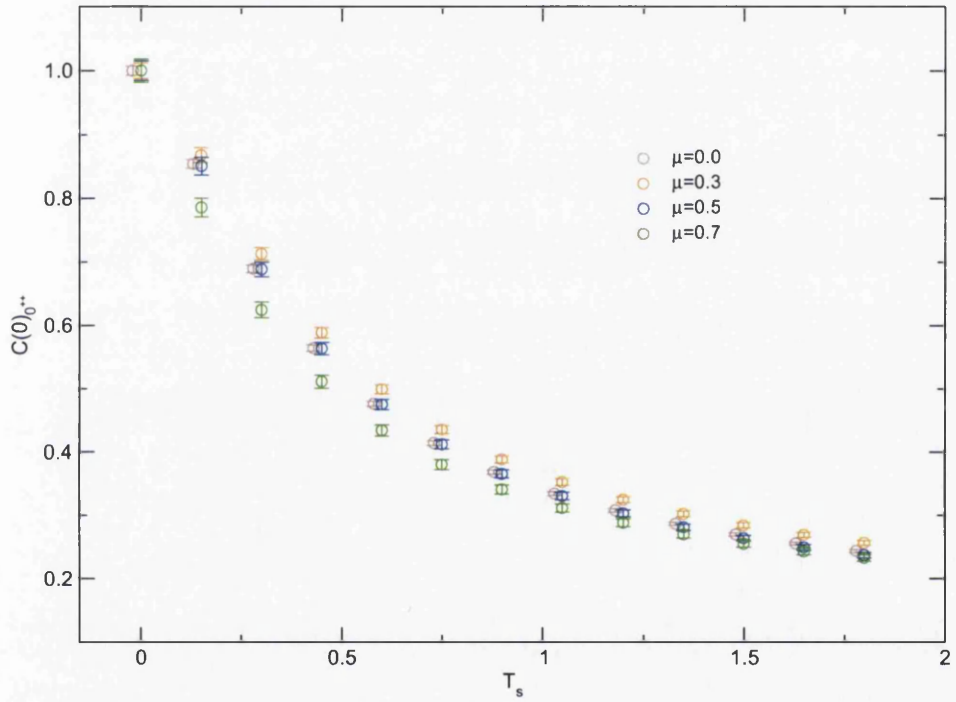

Figure 5.1: Effects of APE smearing on $C(0)$ for the basic 0^{++} operator at $\mu = 0.0, 0.3, 0.5, 0.7$. Note that each curve has been normalised by its unsmeared value, and that the $\mu = 0$ data has been slightly shifted by a negative T_s to aid legibility. It is clear that whilst the $\mu = 0.3$ data is slightly less affected by a given set of APE smears, and the $\mu = 0.7$ slightly more so, such changes are small.

Figure 5.1 shows the effect of different levels of APE smearing on the amplitude, or $C(t = 0)$, of the basic 0^{++} correlator. In contrast to the study of Lombardo et al. any differences with μ are at best subtle. The $\mu = 0.3$ amplitude appears to be slightly less affected by a given weight of smearing and the $\mu = 0.7$ slightly more. However there seems to be no difference between the amplitude in the vacuum superfluid phase.

The effects of smearing on the effective mass as measured by the basic scalar operator is presented in figure 5.2. Values for $t = 0 - 4$ are shown separately, with the lower x-axis labelling them. This is not a continuous axis, and the data is grouped to the right of its corresponding t value. Each colour of continuous line corresponds to different number of smearing steps, $N_s = 1-6$, and the position along the line is the total smearing weight $T_s = N_s \times \lambda$ which runs from $0 - 1.8$. The upper x-axis displays these T_s values. The points with error bars correspond to the effective masses at the values used in the mass fits, that of $N_s = 2$ $\lambda = 0.15$ (orange) and $N_s = 4$ $\lambda = 0.15$ (green). The brown points are the m_{eff} for the diagonalised operator, which whilst it does not have a set level of smearing, has been included for comparison. The grey horizontal line shows the mass obtained from fitting a cosh form to the diagonalised correlator, with its associated error bars given by the dotted lines.

The presented data shows that effective mass of the basic 0^{++} operator has a complex relation to the applied level of smearing. It does not appear to affect the size of the statistical errors and the simplistic picture that it purely reduces contamination from excited states is not evident with the current level of statistics for the basic operator. However the remark that some smearing improves the picture is clearly true, as the points are much more aligned for any non-zero value of T_s. The $t = 1$ value for the diagonalised correlator is evidently lower than the values for the two (of the four) operators shown here which go into its construction, and therefore the procedure, which is set up to minimise this quantity, is working. It does not however appear to have produced a noticeably better correlator, at least in terms of the effective mass. The large uncertainties are a clear sign that the states are not well resolved at even moderate t, and so it is perhaps unsurprising that combining unresolved operators would create an equally unresolved one.

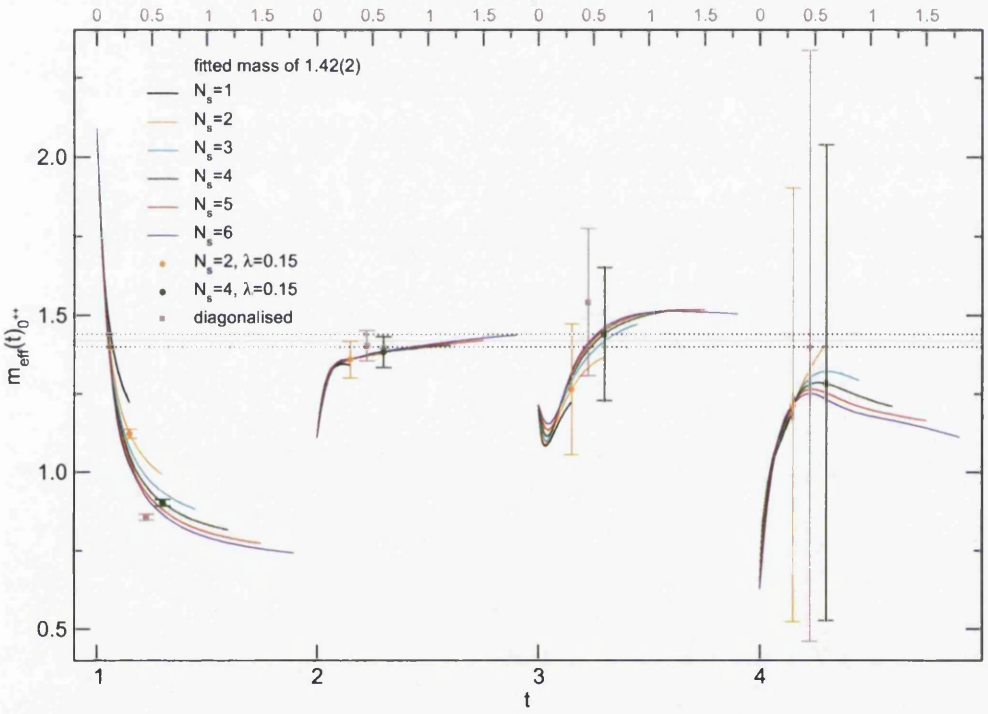

Figure 5.2: Effects of smearing on the $\mu = 0\ 0^{++}$ effective mass, m_{eff}. Values for $t = 0 - 4$ are shown separately, with the lower x-axis labelling them. Note that this is not a continuous axis, and the data is grouped to the right of its corresponding t value. Each colour of continuous line corresponds to different number of smearing steps, $N_s = 1 - 6$, and the position along the line is the total smearing weight $T_s = N_s \times \lambda$ which runs from $0 - 1.8$. The upper x-axis displays these T_s values. The points with error bars correspond to the effective masses at the values used in the mass fits, that of $N_s = 2\ \lambda = 0.15$ (orange) and $N_s = 4\ \lambda = 0.15$ (green). The grey points are the m_{eff} for the diagonalised operator, which does not have a set level of smearing, has been included for comparison. The grey horizontal line shows the fitted mass for this state along with its error bars (dotted lines).

5.1.2 Resolving The Vacuum

The vacuum expectation value of the 0^{++} operator is non-zero and therefore must be subtracted in order to construct a reasonable correlator. This procedure is described in the definition of glueball operators in section 3.3. However if this vacuum expectation value is not adequately determined there will be some residual c that will appear as a time independent constant term in the measured correlator. Due to the exponential behaviour of the correlator it is clear that such a term will always be present for some t close to the centre of the lattice, however if it is smaller than the gauge noise it will not be discernible. Adequately determined therefore just means that this residual is smaller or comparable with the noise floor.

The measured values of the average spatial plaquette at smearing level $N_s = 4$ and $\lambda = 0.15$ as a function of μ are shown in figure 5.3. This quantity is precisely the vacuum expectation value of the basic 0^{++} operator, and so its square is the constant that would appear in the diagonal correlator C_{ii} if no subtraction took place. It exhibits three different behaviours which line up with the three regions identified for this system: i.e. flat for vacuum, an increased value in the superfluid phase and a rapid decrease for large $\mu > 0.6$. This quantity is also related to the gluonic energy density which is proportional to the difference between the average temporal and spatial plaquette and the trace of the energy momentum tensor through the conformal anomaly [52] which is proportional to their sum.

The two insets on the graph show the autocorrelation of the average spatial plaquette and the measured values of the exponential and integrated autocorrelation times, τ_{exp} and τ_{int} (as defined in section 3.4.2). τ_{exp} was estimated by fitting an exponential form to first 15 points of the autocorrelation data and the sum to calculate τ_{exp} was performed until the data went negative. Both the autocorrelation times appear to be the same at the measured level of precision and so shall be referred to interchangeably as τ. It is interesting to note that τ peaks at onset ($\mu = 0.4$) and that if the points at $\mu = 0.38, 0.55$ are ignored then there appears to be different behaviour before and after this

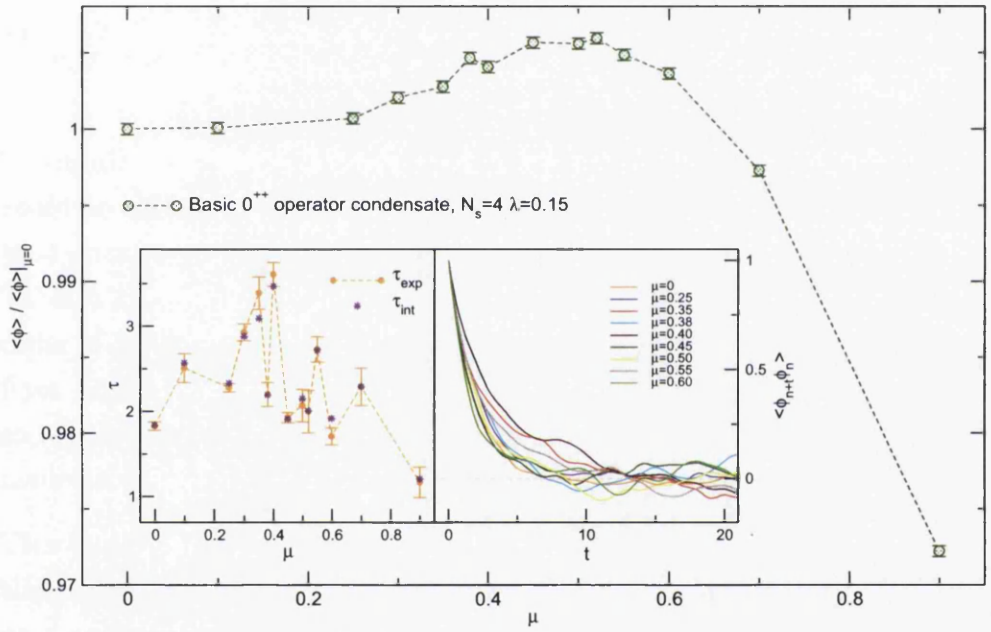

Figure 5.3: The average spatial plaquette, $\langle\phi\rangle$ as a function of μ at $N_S = 4\lambda = 0.15$. This is the vacuum contribution to the basic 0^{++} operator. The right inset shows the autocorrelation of $\langle\phi\rangle$, and the left inset the measured values for the exponential and integrated autocorrelation times, τ_{exp} and τ_{int} respectively.

point. It is important keep in mind that the autocorrelation times are very difficult quantities to measure for small data sets, but they do seem to show that onset appears in the algorithms ability to measure this quantity.

μ	$\langle\phi\rangle^2$	% error
0.00	7543800(1100)	0.01
0.30	7575000(3500)	0.05
0.50	7628500(3400)	0.04
0.70	7502700(4400)	0.06

Table 5.2: Square of the average spatial plaquette at $\mu = 0.0, 0.3, 0.5, 0.7$ and $N_s = 4$ $\lambda = 0.15$. Note that these numbers in common with all presented results have not been normalised by the volume.

To obtain an estimate of the maximum size of any possible residual c that could be expected to appear in the measured 0^{++} basic correlators, the statistical error in the square of average spatial plaquette $\langle\phi\rangle^2$ has been measured. Table 5.2 shows this quantity for a range of μ and it is clear that it is of the order of 1000. Note that for the diagonalised correlators there will be residual from each of the operators that are used with the appropriate weights and so it is harder to obtain an estimate for their size, however it is a reasonable assumption that it should be of a similar order.

The basic scalar correlators for $\mu = 0.35$ and $\mu = 0.38$ are displayed in the upper frame of figure 5.4. It is clear that neither appears to decay as a pure exponential which would appear as a straight line on this plot, an example of which is given by the brown dashed line. The $\mu = 0.35$ $t = 4, 5$ points are negative and so do not appear on the plot. A simple cosh fit to each would result in a large mass difference for a small change in μ although these points are close to onset, so a rapid change may not be unphysical. The curvature makes setting a fit range difficult. A much better explanation of the behaviour of the correlators is obtained when the fit includes a free constant c, which should effectively measure the residual by removing the vacuum contributions. These are the displayed fits. Note that the c is measured to be of order 200 for both correlators but is opposite in sign. This falls well within the expected range for such a residue as it is an order of magnitude smaller than the measured errors in $\langle\phi\rangle^2$. Brown dotted

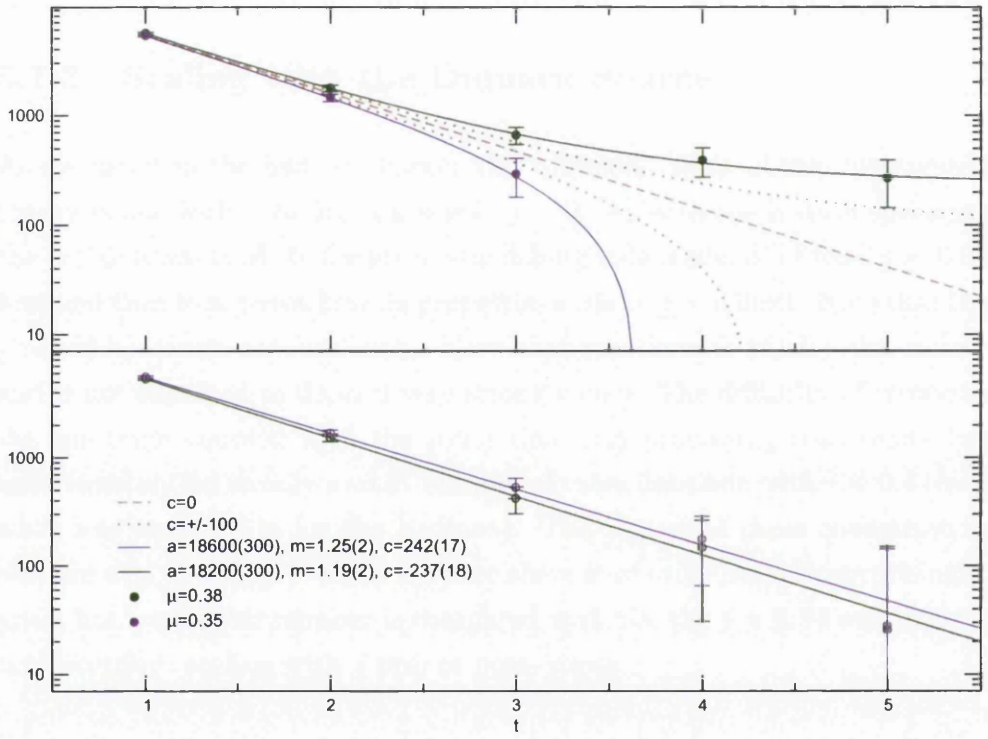

Figure 5.4: $\mu = 0.35, 0.38$ basic 0^{++} correlators and fits with a free constant included. Smearing $N_s = 4, \lambda = 0.15$. The upper frame shows both correlators and their associated fits. The grey dashed lines show a cosh functions with and without an additional constant $c = -100, 100$ for comparison. The lower frame presents the same data, but with the relevant fitted constant subtracted from each correlator. Note the appearance of $t = 5, 6$ $\mu = 0.35$ points, which unmodified were negative and so could not be placed on the upper frame. It is clear that the allowing $c \neq 0$ in the fitting procedure improves the quality of the fit especially for large t.

lines with $c = \pm 100$ are also plotted. The lower frame displays the same data but with the relevant c subtracted from the correlator directly, and clearly shows the appropriateness of such a fit. Over the displayed range of t both correlators appear to decay exponentially and interestingly with very similar values of mass.

5.1.3 Scaling with the Diquark Source

As discussed in the hadron chapter the "physical" limit of the investigated theory is one with zero diquark source $j = 0$. As with the hadron spectrum the decision was made to focus on establishing μ dependence at fixed $j = 0.04$ first and then look to see how its properties scale to $j = 0$ limit. Note that the glueball spectrum requires many more configurations to resolve the masses and is not expected to depend very strongly on j. The difficulty of resolving the spectrum coupled with the usual time and processing constraints has unfortunately led to only a small number of extra data sets with $j \neq 0.4$ (over what was analysed in for the hadrons). The largest of these configuration sets are at $j = 0.06$, $\mu = 0.3, 0.6$ where there is of order 200. Unsurprisingly, given how small this number is compared with the the $j = 0.04$ set, there is no discernible scaling with j pre- or post- onset.

5.2 Results

As with the hadronic data, this exploratory study is unfortunately not high precision and no attempt is made to look at volume or continuum scaling. The aim is to make measurements that inform about the behaviour of the lattice system as μ increases and explore the phase space. The emphasis is on trends and not specific values of properties. Another important point is that with "low statistics", at least compared with the variation, consistency is important measure of how well the physics is resolved. For example, in a regime which is assumed to be stable, neighbouring points give a fairly

independent check on each other, i.e. a small change in μ should only give a small change in the observable. The obvious counter to this is when there are indeed rapid changes in the system.

5.2.1 Glueball Amplitudes

The amplitude of a given correlator is given by the zero time correlation function $C(t = 0)$. The measured 0^{++} and 2^{++} amplitudes from the basic operators at $N_s = 4$ $\lambda = 0.15$ are displayed in figure 5.5. Both sets are normalised by their $\mu = 0$ value and are on different y-axes. Data for the scalar amplitude is displayed both with and without the fitted c subtracted (orange and purple respectively). Note that it makes little sense to compare the raw amplitudes of the diagonalised correlators, as any variation is likely to largely be down to the make-up of each operator as opposed to a physical property. However the proportion of each basic operator in constructed diagonalised operator could be looked at, as the preferentially selected operator will be the one that most resembles the state.

The scalar amplitude appears to be constant in the vacuum phase up until onset $\mu = 0.4$, although from $\mu = 0.3$ the signal becomes noisier. Post-onset the amplitude steadily decreases until it reaches about 85% of its vacuum value at $\mu = 0.6$. After this point it remains consistently low. There is little qualitative difference with or without the vacuum corrections. It is interesting to note that these three distinct behaviours tie-up closely with the predicted "phases" of the system. This behaviour also agrees at least qualitatively with the observations of [78]. Lombardo *et al.* found that the scalar amplitude remained constant until onset where they observed a noticeable peak; a feature not incompatible with this work, especially for the c-subtracted data. This peak was attributed to the fact that the system is undergoing a phase change at onset and because the vacuum subtracted

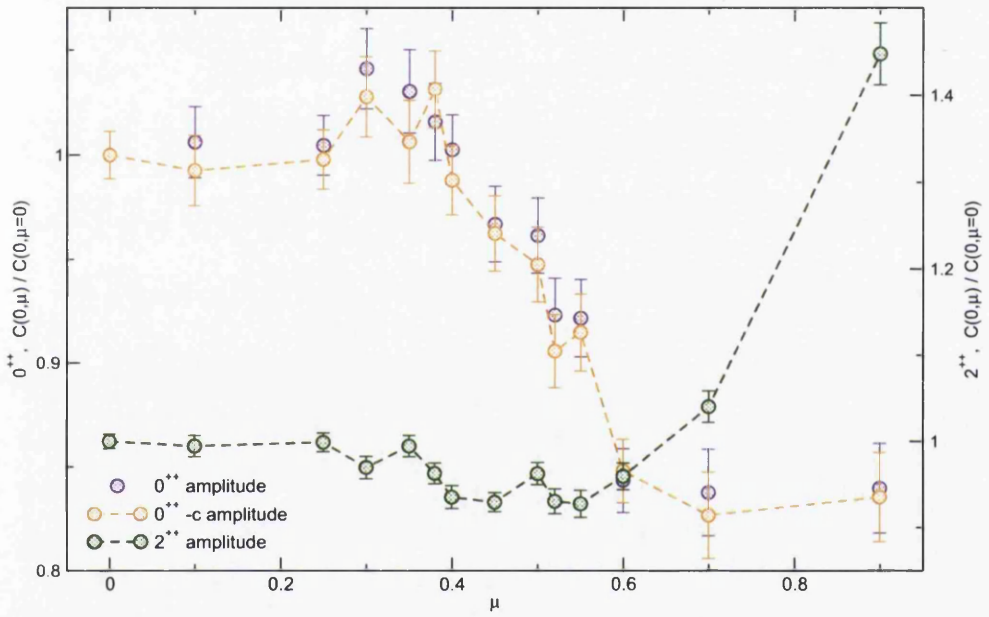

Figure 5.5: 0^{++} and 2^{++} amplitudes as a function of μ obtained from basic $N_s = 4$ $\lambda = 0.15$ operators. The 0^{++} data includes both "corrected" values (orange), where the fitted free parameter was taken into account, and the directly measure value (purple). Note that all the data sets are normalised by their $\mu = 0$ value and that the two states are displayed on different y-axes, where the left axis applies to the 0^{++} data and the right the 2^{++}.

amplitude is defined as

$$C(0) = \frac{1}{N_t} \sum_{\tau=0}^{N_t-1} (< \phi^{0^{++}}(\tau)^2 > - < \phi^{0^{++}}(\tau) >^2) \tag{5.1}$$

and hence it is related to the plaquette susceptibility, which is a standard indicator of criticality. Beyond onset they observed a rapid drop to a low value, the rate of which is difficult to compare between different physical systems with different lattice spacings. At high μ they observed the amplitude approach the value of the quenched theory, which is a clear indication of saturation freezing out the sea quarks. Note that in the system investigated here, saturation effects have been observed but only at values of μ much higher than in this study $\mu \sim 1.5$ [52].

The 2^{++} amplitude in figure 5.5, also appears to show three regimes in μ. It has a vacuum value and a superfluid value which is approximately 7% smaller, and it appears to interpolate between them just before onset at $\mu \sim 0.38$. In the high density phase $\mu > 0.55$ the tensor amplitude grows rapidly.

5.2.2 The Scalar Glueball Mass

The mass results from cosh fits (with $c = 0$) to the basic and diagonalised scalar glueball correlators are presented in figure 5.6 (red and green points respectively). The basic operator was fitted over a fixed time interval $t = [1 : 15]$ and the diagonalised operators with a more selective one, $t = [1 : 4, 5]$. The exceptions are the points at $\mu = 0.5, 0.52$ which were fitted over $t = [2 : 5]$.

The obtained masses track each other very closely, and whilst the masses from the "improved" correlators are lower at a few points, there is little evidence that they offer a significant advantage for this state. The error bars are similar for both data sets with the diagonalised ones being in general smaller, although it is difficult to attribute this to anything other than the different fitting methods. The only major difference between the two data

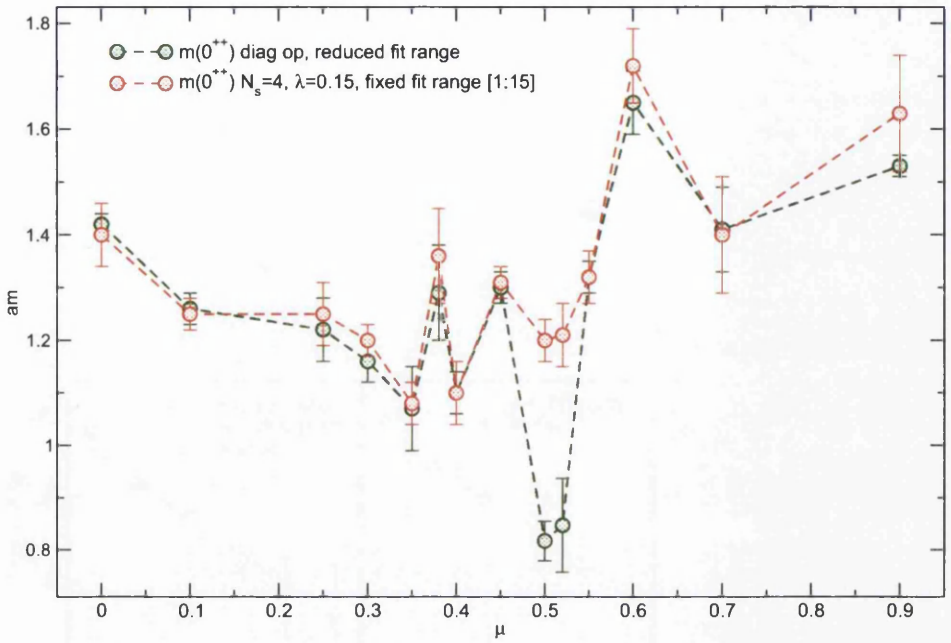

Figure 5.6: 0^{++} masses as a function of μ from cosh fits to basic $N_S = 4\,\lambda = 0.15$ (red), and diagonalised (green) operators. Note that the basic operators were fitted over a fixed t interval [1:15].

sets is at $\mu = 0.50$ and $\mu = 0.52$ where the diagonalised correlator measures a much lighter mass. The correlators for these two points are shown in figure 5.7. The three columns of plots, reading left to right, show the basic, diagonalised, and both together with vacuum corrections. The first two columns neatly demonstrate that this large mass difference is due to the fact that the improved correlators are fitted to an interval starting at $t = 2$. It is clear from the plots that these fits starting at $t = 2$ explain more of the data at these values of μ, note that this is not generally true.

From the these standard cosh fits the μ dependence of the scalar glueball mass is unclear. It appears to drop from its $\mu = 0$ value and then stabilise from $\mu = 0.1 \rightarrow 0.3$. Large fluctuations are visible as the system approaches and moves through onset. The most striking features then occur as mass appears to drop to a much lighter value at $\mu = 0.5$ and $\mu = 0.52$, and then increase well beyond its $\mu = 0$ value, peaking at $\mu = 0.6$. It remains heavy for the final two points.

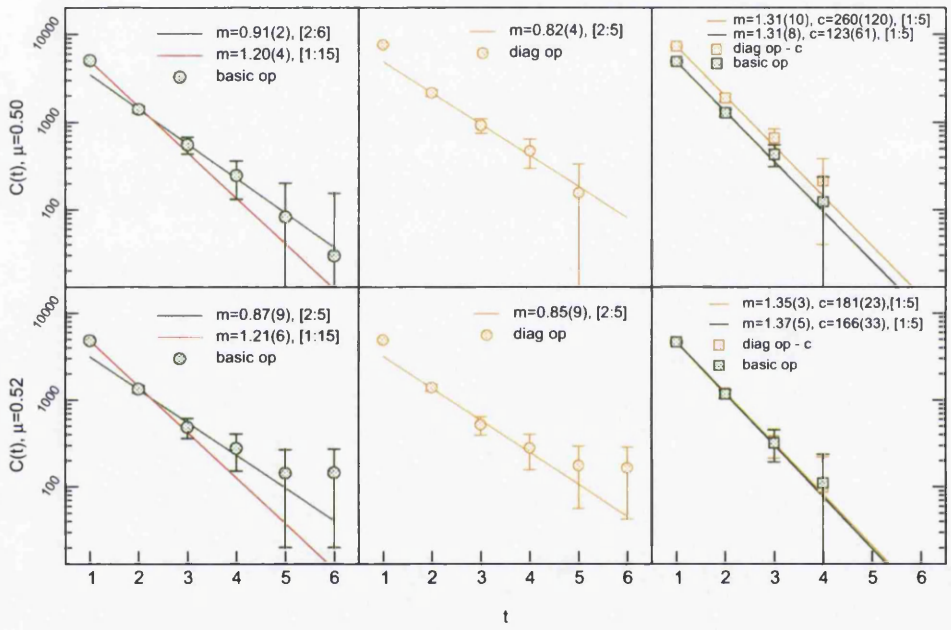

Figure 5.7: 0^{++} correlators at $\mu = 0.50$ (upper row) and $\mu = 0.52$ (lower row). The leftmost column contains basic correlators at $N_s = 4$ $\lambda = 0.15$, the central column the diagonalised correlators and the right both correlators with the fitted constant subtracted. Note that t starts from 1, not zero.

The Scalar Glueball Mass fitted with a Vacuum Residual

The mass results from cosh fits with a free constant to take account of any vacuum residual are presented in figure 5.8. Note that all of these fits are performed over the range $t = [1 : 5]$ with the exceptions of $\mu = 0.6, 0.9$ which were better fitted by the $t = [1 : 4]$ interval. The insets shows the fitted values for c. They appear to be randomly distributed around zero and are in general an order of magnitude smaller than measured error in the subtracted vacuum contribution as discussed in section 5.1.2.

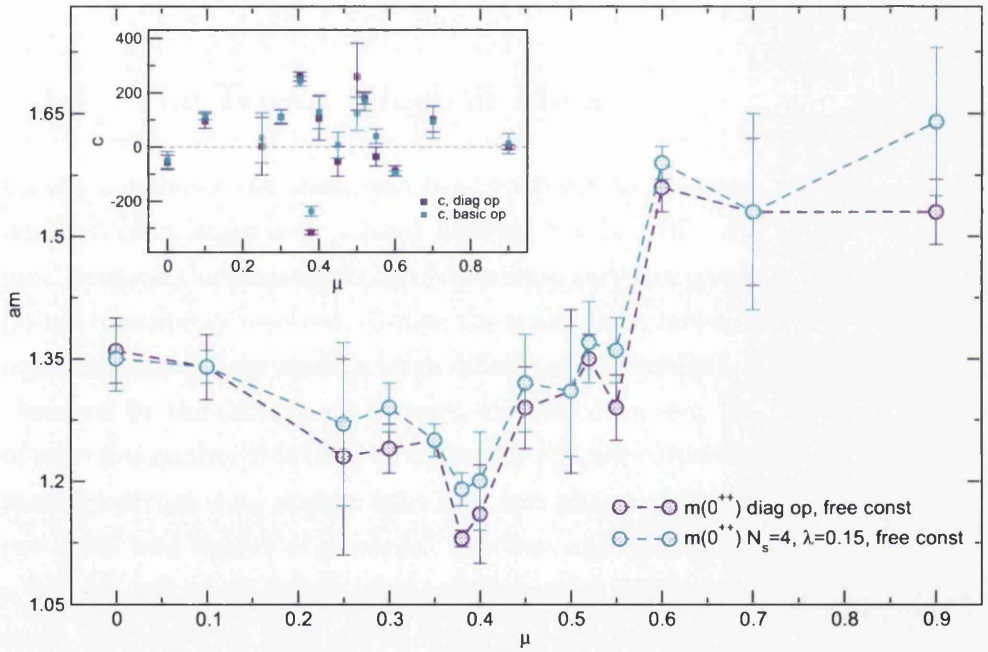

Figure 5.8: 0^{++} masses as a function of μ from cosh fits with an additional constant parameter to basic $N_S = 4\ \lambda = 0.15$ operators (cyan), and diagonalised operators (violet). The inset shows the fitted values for c.

The modification of the fit function has had a smoothing effect of the measured mass spectrum. Most notably the the $\mu = 0$ mass has been reduced to much closer to the $\mu = 0.1$ point and the low mass points around $\mu = 0.5$ are no longer light compared with the states mass in the vacuum. From this data it appears that the scalar glueball has two distinct mass regimes with some evidence for a feature around onset. It remains approximately constant

in the vacuum phase, becomes lighter around onset, and then returns to its vacuum value until $\mu = 0.6$ where it becomes heavy and appears to remain so.

These observations contrast with the work of Lombardo *et al.* who found that the scalar state became very light in the superfluid phase. They also noticed that the separation of the state from vacuum contributions is not a trivial matter. It is possible that there is indeed a lighter mode that is being swamped by an excited state and the vacuum after onset, but an in depth, more specialised study would be required to show this.

5.2.3 The Tensor Glueball Mass

Figure 5.9 shows the mass results of cosh fits to the tensor basic and diagonalised correlators over a fixed interval $t = [1 : 15]$. Such a crude fit was used because the measured correlators were very noisy, with only the $t = 1, 2$ points reasonably resolved. Unlike the scalar data however, the improved diagonalised operators made a large difference, especially post-onset, as can be observed by the differences between the two data sets. With the correlators of such low quality it is hard to make any concrete observations, although the mass spectrum does appear split into two phases, with the 2^{++} being heavy pre-onset and lighter afterwards. The two apparently exceptional points at $\mu = 0.38$ and $\mu = 0.52$ are easy to ignore with the current resolution of this state, as their error bars and the general confidence levels do not sufficiently separate them from their neighbours.

5.3 Discussion and Outlook

The main observations from the glueball spectrum are:

- Both the scalar and the tensor glueball amplitudes show clearly different behaviour in the three μ regimes, and that the gluon sector is

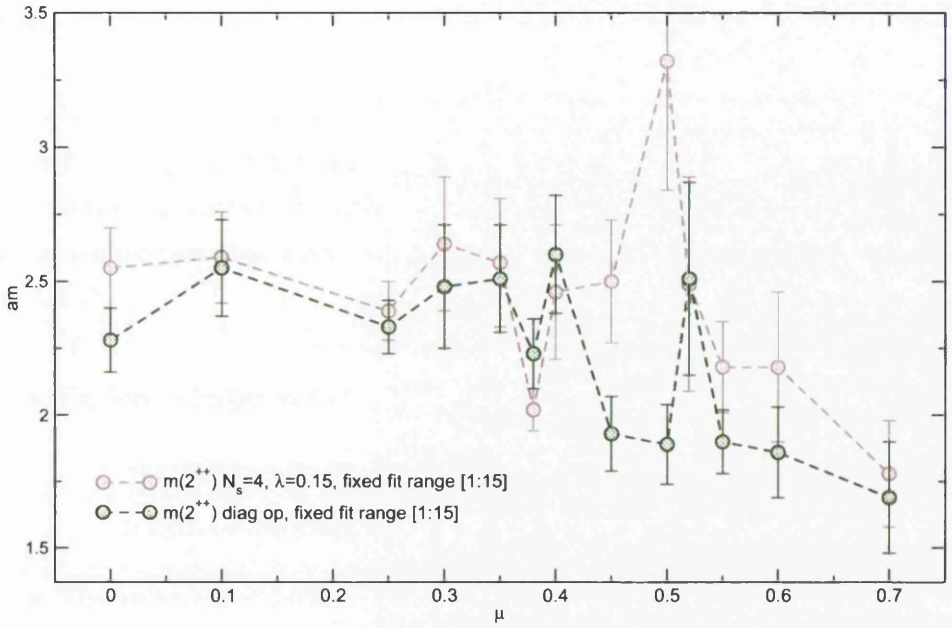

Figure 5.9: 2^{++} masses as a function of μ from cosh fits to basic $N_S = 4\lambda = 0.15$ (brown), and diagonalised (green) operators. Note that the both operators were fitted over a fixed t interval [1:15].

heavily modified by the changes in the theory for increasing chemical potential.

- In order to fit the scalar glueball, its overlap with the vacuum must be carefully resolved. This is especially problematic in the superfluid phase, since for the simple operator used in this study, the overlap with the vacuum is largest and the glueball amplitude (essentially a measure of how well the operator couples to the state) is decreasing in this phase.

- The tensor mass is difficult to resolve with simple operators in a non-ideal system, however it does appear to be qualitatively different in the superfluid phase from the vacuum.

Outlook

The gluonic spectrum is not easy to measure well, the observables in general suffer from large fluctuations, a high noise floor and do not overlap strongly with simple operators. To take the glueball project forward it is clear more of the techniques that have dramatically improved glueball spectroscopy in full QCD.

- Explore a larger variety of operators, choose/diagonalise to:
  - minimise vacuum contributions in the scalar channel
  - maximise overlap for the superfluid phase
- The volume and lattice spacing dependence of all the observables needs to be checked, specifically the transition points of onset and beginning of the high μ phase to see how they scale.
- Finer lattices in the temporal direction would lead to much better fits and help to resolve vacuum residuals

Finally there are other glueball channels that could be investigated.

Chapter 6

Conclusions

Numerical techniques were used to study the spectrum of 2-colour quantum chromodynamics on the lattice as it responded to an increasing chemical potential.

Hadronic spectroscopy was performed with all-to-all quark propagators, constructed using the Dublin method and were diluted in time, spin and colour. The mass hierarchy of the pion and the rho was observed to flip in the superfluid phase. Evidence was found for meson baryon mixing, and Higgs and Goldstone states associated with the spontaneous symmetry breaking at onset and in the superfluid phase were investigated. Additionally kaonic states were constructed from partially quenched propagators and provided evidence for bound kaons in nuclear matter.

Glueball operator construction was discussed and applied in the scalar and tensor channels. The vacuum overlap of the scalar operator was measured and subtracted from the correlators. It was observed that this was not sufficient to obtain consistent fits, especially around onset and in the superfluid phase. Therefore this residual constant was added into the fit. This resulted in a scalar glueball mass that remained constant until high μ but shows a dip at onset. The tensor glueball was observed to be ill-fitted by the chosen operators in the vacuum, but was better resolved by the diagonalised operators

in the superfluid phase. Finally the amplitudes of both states were observed to display different behaviour in the three phases.

Like all lattice based work, addition simulations at different a and volumes need to be carried out to see how properties will scale. Additionally with the observed noise levels there is plenty of scope for increasing accuracy, increasing confidence in the observed features and crucially furthering the investigation of the high μ regime.

Bibliography

[1] J. B. Kogut, M. A. Stephanov, D. Toublan, J. J. M. Verbaarschot, and A. Zhitnitsky, Nucl. Phys. **B582**, 477 (2000), hep-ph/0001171.

[2] H. Fritzsch, M. Gell-Mann, and H. Leutwyler, Phys. Lett. **B47**, 365 (1973).

[3] Y. Aoki, G. Endrodi, Z. Fodor, S. D. Katz, and K. K. Szabo, Nature **443**, 675 (2006), hep-lat/0611014.

[4] Y. Aoki, Z. Fodor, S. D. Katz, and K. K. Szabo, Phys. Lett. **B643**, 46 (2006), hep-lat/0609068.

[5] M. Cheng *et al.*, Phys. Rev. **D74**, 054507 (2006), hep-lat/0608013.

[6] B. B. Back *et al.*, Nucl. Phys. **A757**, 28 (2005), nucl-ex/0410022.

[7] STAR, J. Adams *et al.*, Nucl. Phys. **A757**, 102 (2005), nucl-ex/0501009.

[8] BRAHMS, I. Arsene *et al.*, Nucl. Phys. **A757**, 1 (2005), nucl-ex/0410020.

[9] PHENIX, K. Adcox *et al.*, Nucl. Phys. **A757**, 184 (2005), nucl-ex/0410003.

[10] M. G. Alford, K. Rajagopal, and F. Wilczek, Nucl. Phys. **B537**, 443 (1999), hep-ph/9804403.

[11] T. Schafer and F. Wilczek, Phys. Rev. Lett. **82**, 3956 (1999), hep-ph/9811473.

[12] D. H. Rischke, Prog. Part. Nucl. Phys. **52**, 197 (2004), nucl-th/0305030.

[13] M. G. Alford, J. A. Bowers, and K. Rajagopal, J. Phys. **G27**, 541 (2001), hep-ph/0009357.

[14] K. Rajagopal and F. Wilczek, (2000), hep-ph/0011333.

[15] J. A. Bowers and K. Rajagopal, Phys. Rev. **D66**, 065002 (2002), hep-ph/0204079.

[16] R. Rapp, T. Schafer, E. V. Shuryak, and M. Velkovsky, Phys. Rev. Lett. **81**, 53 (1998), hep-ph/9711396.

[17] R. Aloisio, V. Azcoiti, G. Di Carlo, A. Galante, and A. F. Grillo, Nucl. Phys. **B606**, 322 (2001), hep-lat/0011079.

[18] J. B. Kogut, D. K. Sinclair, S. J. Hands, and S. E. Morrison, Phys. Rev. **D64**, 094505 (2001), hep-lat/0105026.

[19] S. Hands, I. Montvay, L. Scorzato, and J. Skullerud, Eur. Phys. J. **C22**, 451 (2001), hep-lat/0109029.

[20] M. G. Alford, K. Rajagopal, and F. Wilczek, Phys. Lett. **B422**, 247 (1998), hep-ph/9711395.

[21] J. Berges and K. Rajagopal, Nucl. Phys. **B538**, 215 (1999), hep-ph/9804233.

[22] K. Wilson, Phys. Rev. **D10**, 2445 (1974).

[23] B. Bunk, M. Della Morte, K. Jansen, and F. Knechtli, Nucl. Phys. **B697**, 343 (2004), hep-lat/0403022.

[24] F. Maresca and M. Peardon, (2004), hep-lat/0411029.

[25] P. Hasenfratz and F. Karsh, Phys. Lett. **125B**, 308 (1983).

[26] R. V. Gavai, Phys. Rev. D **32**, 519 (1985).

[27] W. Bietenholz and U. J. Wiese, Phys. Lett. **B426**, 114 (1998), hep-lat/9801022.

[28] M. A. Stephanov, Phys. Rev. Lett. **76**, 4472 (1996), hep-lat/9604003.

[29] G. Akemann, J. C. Osborn, K. Splittorff, and J. J. M. Verbaarschot, Nucl. Phys. **B712**, 287 (2005), hep-th/0411030.

[30] S. Bergkvist, P. Henelius, and A. Rosengren, Reduction of the sign problem using the meron-cluster approach, 2003.

[31] S. Chandrasekharan, Nuclear Physics B - Proceedings Supplements **94**, 71 (2001).

[32] I. M. Barbour, S. E. Morrison, E. G. Klepfish, J. B. Kogut, and M.-P. Lombardo, Nucl. Phys. Proc. Suppl. **60A**, 220 (1998), hep-lat/9705042.

[33] Z. Fodor and S. D. Katz, Phys. Lett. **B534**, 87 (2002), hep-lat/0104001.

[34] QCD-TARO, P. de Forcrand *et al.*, Nucl. Phys. Proc. Suppl. **73**, 477 (1999), hep-lat/9810057.

[35] A. Hart, M. Laine, and O. Philipsen, Phys. Lett. **B505**, 141 (2001), hep-lat/0010008.

[36] C. R. Allton *et al.*, Phys. Rev. **D68**, 014507 (2003), hep-lat/0305007.

[37] R. V. Gavai and S. Gupta, Phys. Rev. **D71**, 114014 (2005), hep-lat/0412035.

[38] M.-P. Lombardo, Nucl. Phys. Proc. Suppl. **83**, 375 (2000), hep-lat/9908006.

[39] P. de Forcrand and O. Philipsen, Nucl. Phys. **B642**, 290 (2002), hep-lat/0205016.

[40] M. D'Elia and M.-P. Lombardo, Phys. Rev. **D67**, 014505 (2003), hep-lat/0209146.

[41] V. Azcoiti, G. Di Carlo, A. Galante, and V. Laliena, JHEP **12**, 010 (2004), hep-lat/0409157.

[42] A. Roberge and N. Weiss, Nucl. Phys. **B275**, 734 (1986).

[43] M. G. Alford, A. Kapustin, and F. Wilczek, Phys. Rev. **D59**, 054502 (1999), hep-lat/9807039.

[44] S. Kratochvila and P. de Forcrand, PoS **LAT2005**, 167 (2006), hep-lat/0509143.

[45] G. Aarts and I.-O. Stamatescu, JHEP **09**, 018 (2008), 0807.1597.

[46] S. Hands, J. B. Kogut, M.-P. Lombardo, and S. E. Morrison, Nucl. Phys. **B558**, 327 (1999), hep-lat/9902034.

[47] M. A. Halasz, J. C. Osborn, and J. J. M. Verbaarschot, Phys. Rev. D **56**, 7059 (1997).

[48] J. B. Kogut, D. Toublan, and D. K. Sinclair, Nucl. Phys. **B642**, 181 (2002), hep-lat/0205019.

[49] G.-f. Sun, L. He, and P. Zhuang, Phys. Rev. **D75**, 096004 (2007), hep-ph/0703159.

[50] S. Muroya, A. Nakamura, and C. Nonaka, Phys. Lett. **B551**, 305 (2003), hep-lat/0211010.

[51] B. Alles, M. D'Elia, and M. P. Lombardo, Nucl. Phys. **B752**, 124 (2006), hep-lat/0602022.

[52] S. Hands, S. Kim, and J.-I. Skullerud, (2006), hep-lat/0604004.

[53] S. Hands *et al.*, Eur. Phys. J. **C17**, 285 (2000), hep-lat/0006018.

[54] F. J. Dyson, J. Mathematical Phys. **3**, 1199 (1962).

[55] J. J. M. Verbaarschot, Phys. Rev. Lett. **72**, 2531 (1994), hep-th/9401059.

[56] S. Hands and D. N. Walters, Phys. Rev. **D69**, 076011 (2004), hep-lat/0401018.

[57] J.-I. Skullerud, S. Ejiri, S. Hands, and L. Scorzato, Prog. Theor. Phys. Suppl. **153**, 60 (2004), hep-lat/0312002.

[58] J. Foley *et al.*, Comput. Phys. Commun. **172**, 145 (2005), hep-lat/0505023.

[59] C. J. Morningstar and M. J. Peardon, Phys. Rev. **D56**, 4043 (1997), hep-lat/9704011.

[60] B. Berg and A. Billoire, Nucl. Phys. **B226**, 405 (1983).

[61] APE, M. Albanese *et al.*, Phys. Lett. **B192**, 163 (1987).

[62] C. Morningstar and M. J. Peardon, Phys. Rev. **D69**, 054501 (2004), hep-lat/0311018.

[63] F. D. R. Bonnet, P. Fitzhenry, D. B. Leinweber, M. R. Stanford, and A. G. Williams, Phys. Rev. **D62**, 094509 (2000), hep-lat/0001018.

[64] C. J. Morningstar and M. J. Peardon, Phys. Rev. **D60**, 034509 (1999), hep-lat/9901004.

[65] S. Basak *et al.*, Phys. Rev. **D76**, 074504 (2007), 0709.0008.

[66] R. Miller, Biometrica **61** (1-15).

[67] B. A. Berg, (2004), cond-mat/0410490.

[68] P. Marenzoni, L. Pugnetti, and P. Rossi, Phys. Lett. **B315**, 152 (1993), hep-lat/9306013.

[69] S. Hands, P. Sitch, and J.-I. Skullerud, Phys. Lett. **B662**, 405 (2008), 0710.1966.

[70] S. Hands, B. Lucini, and S. Morrison, Phys. Rev. **D65**, 036004 (2002), hep-lat/0109001.

[71] S. Hands, S. Kim, and J.-I. Skullerud, Eur. Phys. J. **A31**, 787 (2007), nucl-th/0609012.

[72] J. T. Lenaghan, F. Sannino, and K. Splittorff, Phys. Rev. **D65**, 054002 (2002), hep-ph/0107099.

[73] CERES-Collaboration, B. Lenkeit *et al.*, Nucl. Phys. **A661**, 23 (1999), nucl-ex/9910015.

[74] P. Giudice and S. Hands, Nucl. Phys. **B789**, 111 (2008), hep-lat/0703001.

[75] T. Schafer, Phys. Rev. **D65**, 094033 (2002), hep-ph/0201189.

[76] T. Yamazaki and Y. Akaishi, RIKEN-AF-NP-414.

[77] A. N. Ivanov, P. Kienle, J. Marton, and E. Widmann, (2005), nucl-th/0512037.

[78] M. P. Lombardo, M. L. Paciello, S. Petrarca, and B. Taglienti, (2007), arXiv:0710.3251 [hep-lat].